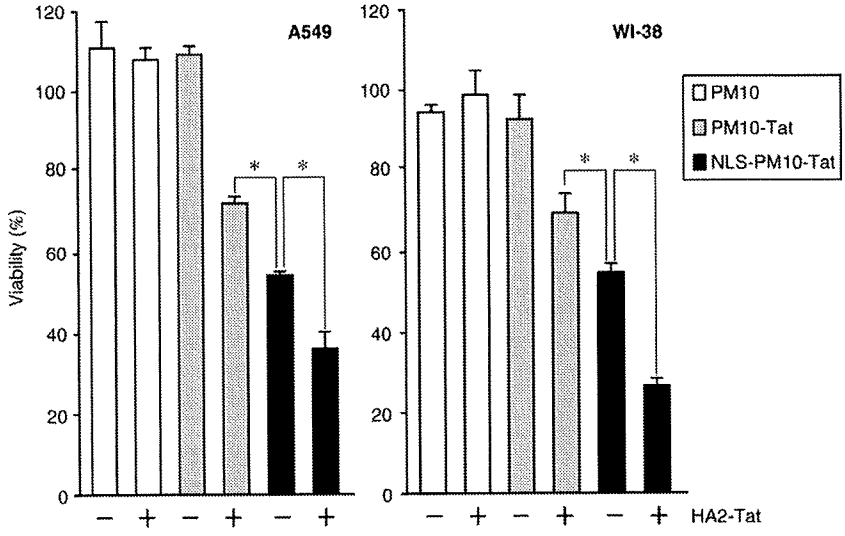

Fig. 3. Nuclear targeting potentiates the cytostatic effect of PM10. All peptides used in this study were purchased from GL Biochem Ltd. (Hiroshima, Japan) with confirmed purities >90% by HPLC and mass spectrography. The sequences of these peptides were GLFEAIEGFIENGWEGMIDGWYG**YGRKKRRQRRR** for HA2–Tat, ETFSDLWKLL for PM10, ETFSDLWKLL**YGRKKRRQRRR** for PM10–Tat and PKKKRKVETFSDLWKLL**YGRKKRRQRRR** for NLS–PM10–Tat. Tat and NLS are shown in boldface and underlined, respectively. A549 or WI-38 cells were seeded into 96-well tissue culture plates (Nalge Nunc International) at 1.0×10^4 cells/well. After incubation for 24 h at 37 °C, the cells were treated with PM10, PM10–Tat or NLS–PM10–Tat at 6 μM (for A549 cells) or 12 μM (for WI-38 cells) in the presence or absence of HA2–Tat (5 μM). After 6 h (for A549 cells) or 24 h (for WI-38 cells), cell viability was determined with the use of WST-8 assay (Nakalai Tesque Inc., Kyoto, Japan) according to the manufacturer's protocol. Data are presented as the mean±SD of triplicate assays. Statistical treatment of the data was performed according to Student's *t* test for two populations (*$p<0.01$).

microscopy (Fig. 2). Co-treatment of HeLa cells with NLS–VENUS–Tat and HA2–Tat resulted in nuclear localization of VENUS, co-localized with Hoechst 33342-stained nuclei. This finding documents that Tat–cargo can be selectively delivered to the nucleus by using HA2 and NLS peptides. Although several groups have attempted to deliver macromolecular drugs to specific organelles, they used PTDs conjugated only with an organelle-targeting signal, such as NLS or mitochondria-targeting signal.[23,24,25] Our data revealed that NLS–VENUS–Tat was entrapped within the endosomal vesicles, with no detectable fluorescence derived from VENUS found in the nucleus. This indicates that organelle targeting by signal-fused PTD–cargo alone does not allow efficient migration into the targeted organelle in the absence of an endosome-escape strategy. Although the influence of the use of different cell types, fluorescent dye, cargo, incubation time and so on could not be excluded as contributing to targeting inability, we found that nuclear transport efficiency could be augmented by combining PTD, HA2 and NLS peptides. Furthermore, our results imply that macromolecules could be delivered into other organelles, such as mitochondria, endoplasmic reticulum and peroxisomes, using different organelle-targeting signal sequences. To this end, we are currently developing novel intracellular drug delivery systems that can target macromolecules into different organelles in a manner analogous to our nuclear targeting techniques.

Nuclear targeting enhances the cytostatic activity of anti-MDM2 peptide aptamer

Next, we tested the utility of our nuclear targeting method using the MDM2-binding peptide aptamer, PM10, which is a p53-derived peptide corresponding to a sequence within the MDM2-binding domain. Kanovsky *et al.* reported that PTD-mediated intracellular delivery of PM10 could reactivate p53 and induce p53-mediated apoptosis of tumor cells with wild-type p53.[11] Under physiological conditions, growth-suppressive and proapoptotic activity of p53 is inhibited by MDM2, which binds p53 and negatively regulates its activity and stability.[16] Recent reports indicated that prevention of p53–MDM2 binding activates the p53 signaling pathway and induces p53-dependent apoptosis in cancer cells possessing wild-type p53.[12,14,15] In addition, the abrogation of p53–MDM2 binding mediates a cytostatic effect and cell cycle arrest in proliferating normal cells.[13,15,17] Because PM10 seems to bind nuclear-localized MDM2 and inhibits MDM2-inducible ubiquitination and degradation of p53, we hypothesized that the nuclear targeting method using HA2 and NLS peptides would enhance its cytotoxicity. To test this, we investigated the effects of treatment with PM10 on cell viability using A549 (human lung adenocarcinoma) and WI-38 (human lung-derived embryonic fibroblast) cells, which possess wild-type p53 (Fig. 3). In A549 and WI-38 cells treated with PM10, Tat-fused PM10 (PM10–Tat) grew vigorously. However, co-treatment with HA2–Tat and PM10–Tat together markedly inhibited A549 and WI-38 cell growth. Furthermore, A549 and WI-38 cells co-treated with HA2–Tat and NLS-fused PM10–Tat (NLS–PM10–Tat) showed greater growth inhibition compared with those treated with NLS–PM10–Tat alone. According to a report from the developers of PM10, although transduction of PTD-fused PM10 (PM10-PTD) into cancer cells could induce tumor cell death *in vitro* and *in vivo*, a high concentration of PM10-PTD was required to see an effect on cancer

cells.[11,26] In contrast, our nuclear targeting technique using PTD, HA2 and NLS peptides markedly enhanced the nuclear localization of the cargo and the PM10-mediated cytostatic effect at low concentrations of PM10. To the best of our knowledge, this is the first report that nuclear targeting of MDM2-binding peptide aptamers can lead to augmentation of cytostatic activity.

In the present study, we aimed to develop a novel cancer therapeutic approach by controlling apoptotic pathways using peptide-based drugs. Recently, the use of intracellular antibodies (intrabodies) directed to a specific target antigen present in the cell has also been suggested as a therapeutic lead to control the apoptotic pathway.[27,28] Our organelle-targeting strategy does seem able to deliver intrabodies directly to the specific organelle in which disease-related proteins reside. Furthermore, we have generated antibodies for various targeted antigens using a non-immune phage scFv library.[29] Thus, we are also currently developing a novel approach to intracellular therapy combining an organelle-targeting strategy and antibody engineering.

Acknowledgements

This study was supported in part by Grants-in-Aid for Scientific Research (20790156) from the Ministry of Education, Culture, Sports, Science and Technology of Japan; in part by a Health and Labor Sciences Research Grant from the Ministry of Health, Labor and Welfare of Japan; in part by a Grant for Industrial Technology Research Program (03A47016a) from the New Energy and Industrial Technology Development Organization of Japan; and in part by funding from the Takeda Science Foundation.

References

1. Mendoza, F. J., Espino, P. S., Cann, K. L., Bristow, N., McCrea, K. & Los, M. (2005). Anti-tumor chemotherapy utilizing peptide-based approaches—apoptotic pathways, kinases, and proteasome as targets. *Arch. Immunol. Ther. Exp.* **53**, 47–60.
2. Dietz, G. P. & Bahr, M. (2004). Delivery of bioactive molecules into the cell: the Trojan horse approach. *Mol. Cell. Neurosci.* **27**, 85–131.
3. Chauhan, A., Tikoo, A., Kapur, A. K. & Singh, M. (2007). The taming of the cell penetrating domain of the HIV Tat: myths and realities. *J. Controlled Release*, **117**, 148–162.
4. Fretz, M., Jin, J., Conibere, R., Penning, N. A., Al-Taei, S., Storm, G. *et al.* (2006). Effects of Na^+/H^+ exchanger inhibitors on subcellular localisation of endocytic organelles and intracellular dynamics of protein transduction domains HIV-TAT peptide and octaarginine. *J. Controlled Release*, **116**, 247–254.
5. Wadia, J. S., Stan, R. V. & Dowdy, S. F. (2004). Transducible TAT-HA fusogenic peptide enhances escape of TAT-fusion proteins after lipid raft macropinocytosis. *Nat. Med.* **10**, 310–315.
6. Sugita, T., Yoshikawa, T., Mukai, Y., Yamanada, N., Imai, S., Nagano, K. *et al.* (2008). Comparative study on transduction and toxicity of protein transduction domains. *Br. J. Pharmacol.* **153**, 1143–1152.
7. Kaplan, I. M., Wadia, J. S. & Dowdy, S. F. (2005). Cationic TAT peptide transduction domain enters cells by macropinocytosis. *J. Controlled Release*, **102**, 247–253.
8. Han, X., Bushweller, J. H., Cafiso, D. S. & Tamm, L. K. (2001). Membrane structure and fusion-triggering conformational change of the fusion domain from influenza hemagglutinin. *Nat. Struct. Biol.* **8**, 715–720.
9. Skehel, J. J., Cross, K., Steinhauer, D. & Wiley, D. C. (2001). Influenza fusion peptides. *Biochem. Soc. Trans.* **29**, 623–626.
10. Sugita, T., Yoshikawa, T., Mukai, Y., Yamanada, N., Imai, S., Nagano, K. *et al.* (2007). Improved cytosolic translocation and tumor-killing activity of Tat-shepherdin conjugates mediated by co-treatment with Tat-fused endosome-disruptive HA2 peptide. *Biochem. Biophys. Res. Commun.* **363**, 1027–1032.
11. Kanovsky, M., Raffo, A., Drew, L., Rosal, R., Do, T., Friedman, F. K. *et al.* (2001). Peptides from the amino terminal mdm-2-binding domain of p53, designed from conformational analysis, are selectively cytotoxic to transformed cells. *Proc. Natl. Acad. Sci. USA*, **98**, 12438–12443.
12. Vassilev, L. T., Vu, B. T., Graves, B., Carvajal, D., Podlaski, F., Filipovic, Z. *et al.* (2004). *In vivo* activation of the p53 pathway by small-molecule antagonists of MDM2. *Science*, **303**, 844–848.
13. Vassilev, L. T. (2004). Small-molecule antagonists of p53–MDM2 binding: research tools and potential therapeutics. *Cell Cycle*, **3**, 419–421.
14. Tovar, C., Rosinski, J., Filipovic, Z., Higgins, B., Kolinsky, K., Hilton, H. *et al.* (2006). Small-molecule MDM2 antagonists reveal aberrant p53 signaling in cancer: implications for therapy. *Proc. Natl. Acad. Sci. USA*, **103**, 1888–1893.
15. Shangary, S., Qin, D., McEachern, D., Liu, M., Miller, R. S., Qiu, S. *et al.* (2008). Temporal activation of p53 by a specific MDM2 inhibitor is selectively toxic to tumors and leads to complete tumor growth inhibition. *Proc. Natl. Acad. Sci. USA*, **105**, 3933–3938.
16. Kubbutat, M. H., Jones, S. N. & Vousden, K. H. (1997). Regulation of p53 stability by Mdm2. *Nature*, **387**, 299–303.
17. Efeyan, A., Ortega-Molina, A., Velasco-Miguel, S., Herranz, D., Vassilev, L. T. & Serrano, M. (2007). Induction of p53-dependent senescence by the MDM2 antagonist nutlin-3a in mouse cells of fibroblast origin. *Cancer Res.* **67**, 7350–7357.
18. Vives, E., Charneau, P., van Rietschoten, J., Rochat, H. & Bahraoui, E. (1994). Effects of the Tat basic domain on human immunodeficiency virus type 1 transactivation, using chemically synthesized Tat protein and Tat peptides. *J. Virol.* **68**, 3343–3353.
19. Vives, E., Brodin, P. & Lebleu, B. (1997). A truncated HIV-1 Tat protein basic domain rapidly translocates through the plasma membrane and accumulates in the cell nucleus. *J. Biol. Chem.* **272**, 16010–16017.
20. Potocky, T. B., Menon, A. K. & Gellman, S. H. (2003). Cytoplasmic and nuclear delivery of a TAT-derived peptide and a beta-peptide after endocytic uptake into HeLa cells. *J. Biol. Chem.* **278**, 50188–50194.
21. Caron, N. J., Quenneville, S. P. & Tremblay, J. P. (2004). Endosome disruption enhances the functional nuclear delivery of Tat-fusion proteins. *Biochem. Biophys. Res. Commun.* **319**, 12–20.

22. Lundberg, M., Wikstrom, S. & Johansson, M. (2003). Cell surface adherence and endocytosis of protein transduction domains. *Mol. Ther.* **8**, 143–150.
23. Shokolenko, I. N., Alexeyev, M. F., LeDoux, S. P. & Wilson, G. L. (2005). TAT-mediated protein transduction and targeted delivery of fusion proteins into mitochondria of breast cancer cells. *DNA Repair (Amst.)*, **4**, 511–518.
24. Del Gaizo, V. & Payne, R. M. (2003). A novel TAT-mitochondrial signal sequence fusion protein is processed, stays in mitochondria, and crosses the placenta. *Mol. Ther.* **7**, 720–730.
25. Matsushita, M., Tomizawa, K., Moriwaki, A., Li, S. T., Terada, H. & Matsui, H. (2001). A high-efficiency protein transduction system demonstrating the role of PKA in long-lasting long-term potentiation. *J. Neurosci.* **21**, 6000–6007.
26. Michl, J., Scharf, B., Schmidt, A., Huynh, C., Hannan, R., von Gizycki, H. *et al.* (2006). PNC-28, a p53-derived peptide that is cytotoxic to cancer cells, blocks pancreatic cancer cell growth *in vivo*. *Int. J. Cancer*, **119**, 1577–1585.
27. Wheeler, Y. Y., Kute, T. E., Willingham, M. C., Chen, S. Y. & Sane, D. C. (2003). Intrabody-based strategies for inhibition of vascular endothelial growth factor receptor-2: effects on apoptosis, cell growth, and angiogenesis. *FASEB J.* **17**, 1733–1735.
28. Williams, B. R. & Zhu, Z. (2006). Intrabody-based approaches to cancer therapy: status and prospects. *Curr. Med. Chem.* **13**, 1473–1480.
29. Imai, S., Mukai, Y., Nagano, K., Shibata, H., Sugita, T., Abe, Y. *et al.* (2006). Quality enhancement of the non-immune phage scFv library to isolate effective antibodies. *Biol. Pharm. Bull.* **29**, 1325–1330.

Laboratory of Pharmaceutical Proteomics[1], National Institute of Biomedical Innovation (NIBIO), Graduate School of Pharmaceutical Sciences[2], Center of Advanced Medical Engineering and Informatics[3], Osaka University, Osaka, Japan

Effect of protein properties on display efficiency using the M13 phage display system

S. Imai[1, 2], Y. Mukai[1, 2], T. Takeda[1], Y. Abe[1], K. Nagano[1, 2], H. Kamada[1, 3], S. Nakagawa[2], S. Tsunoda[1, 3], Y. Tsutsumi[1, 2, 3]

Received May 15, 2008, accepted May 21, 2008

Shin-ichi Tsunoda, Ph.D., Laboratory of Pharmaceutical Proteomics, National Institute of Biomedical Innovation (NIBIO), 7-6-8 Saito-Asagi, Ibaraki, Osaka 567-0085, Japan
tsunoda@nibio.go.jp

Pharmazie 63: 760–764 (2008) *doi: 10.1691/ph.2008.8132*

The M13 phage display system is a powerful technology for engineering proteins such as functional mutant proteins and peptides. In this system, it is necessary that the protein is displayed on the phage surface. Therefore, its application is often limited when a protein is poorly displayed. In this study, we attempted to understand the relationship between a protein's properties and its display efficiency using the well-known pIII and pVIII type phage display system. The display of positively charged SV40 NLS and HIV-1 Tat peptides on pIII was less efficient than that of the neutrally charged RGDS peptide. When different molecular weight proteins (1.5–58 kDa) were displayed on pIII and pVIII, their display efficiencies were directly influenced by their molecular weights. These results indicate the usefulness in predicting a desired protein's compatibility with protein and peptide engineering using the phage display system.

1. Introduction

Phage display systems have attracted much attention as the best technology to create functional mutant proteins and peptides ever since Smith et al. reported that random peptides could be displayed on the surface of filamentous M13 phage (Smith 1985). Many researchers have applied this system in attempts to create human antibodies and tissue-specific peptides (Schier et al. 1996; Maruta et al. 2003; Imai et al. 2006). Indeed, we have been successful in creating a useful mutant TNF to be used as a drug (Shibata et al. 2004; Yamamoto et al. 2003). Thus, the phage display system has a wide range of applications (Stich et al. 2003; Gourdine et al. 2005; Takashima et al. 2000).

Filamentous M13 phage has a circular single stranded DNA and takes the form of a long tube that consists of eleven kinds of proteins. This virus effectively proliferates upon infection of *E. coli* (Sidhu 2001; Bayer and Feigenson 1985; Kuhn 1987). In the phage display system, a fusion protein composed of target-molecule and coat protein is derived from a phagemid vector, and wild-type phage composition proteins (pI–pXI) are derived from a helper phage genome. These components can make phage libraries that display target-molecules by assembling within the periplasm of *E. coli*. The most useful characteristic of this system is that protein libraries can be displayed easily on the phage surface by inserting gene libraries within the phage genome. Target-molecules are obtained rapidly by the use of an *in vitro* affinity panning procedure that selects and amplifies specific phage clones (Smith 1985).

In the phage display system, target-molecules can be displayed on coat proteins (pIII, pVI, pVII, pVIII, pIX), though generally they are displayed on pIII or pVIII. Displaying 0–1 molecule per phage in the pIII type phage display system is suitable for isolating high-affinity molecules (Chasteen et al. 2006; Keresztessy et al. 2006). Alternatively, ten molecules can be displayed on a phage particle in the pVIII type phage display system to select low-affinity molecules (Verhaert et al. 1999; Kneissel et al. 1999; Lowman 1997).

As described, the phage display system is the most useful tool to create bioactive peptides and functional mutant proteins. However, because the efficiency of display is influenced by the properties of the target protein (molecular weight, electric charge, etc.), poor display often limits its application. Despite this problem, there is little research examining the relationship between display efficiency and a protein's properties. Thus, studies are warranted in order to apply the phage display system effectively. In this report, we prepared phages that displayed proteins of different molecular weights and electric charges to ascertain the relationship between display efficiency and protein properties.

2. Investigations, results and discussion

In this study we examined the relationship between protein properties (molecular weight, electric charge etc.) and the efficiency of display with pIII and pVIII coat proteins of the filamentous M13 phage display system (Fig. 1). To begin with, we prepared phages that displayed different electrically charged peptides on pIII (Fig. 2B) and evalu-

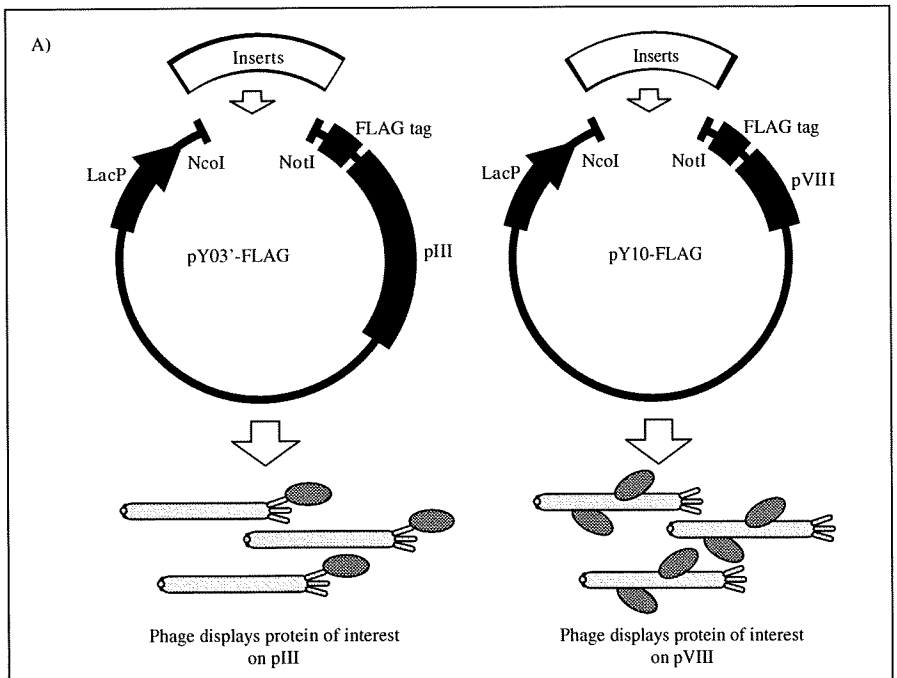

B)

Inserts	Molecular weight (Da)	pI
RGDS peptide (RGDS)	443	6.4
SV40 NLS peptide (PKKKRKV)	883	11.9
HIV-Tat peptide (YGRKKRRQRRR)	1,559	12.8
LacZ-α	11,000	5.2
anti-KDR scFv	25,000	5.0
Importin-α	58,000	5.1

Fig. 1:
Construction of phagemid vectors encoding different proteins or peptides.
A) Different inserts were cloned into pY03′-FLAG and pY10-FLAG phagemid vectors. Phage particles displaying proteins fused to pIII and pVIII were prepared from pY03′-FLAG and pY10-FLAG, respectively. B) Different inserts and their molecular weights

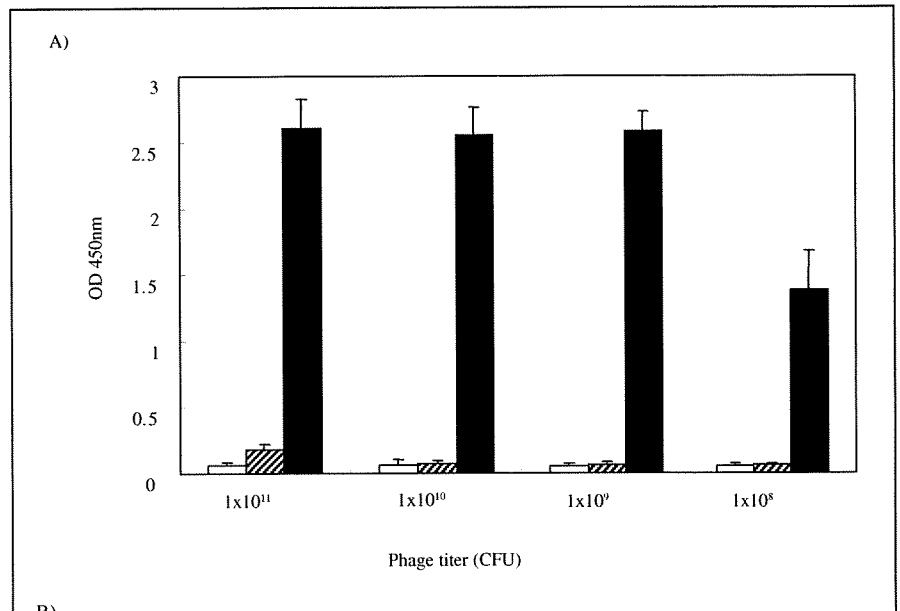

B)

	sequence	M.W. (Da)	pI
□ Tat peptide	YGRKKRRQRRR	1,559	12.8
▨ SV40 NLS	PKKKRKV	883	11.9
■ RGDS peptide	RGDS	433	6.4

Fig. 2:
Influence of the efficiency of peptide-display by the ionic charge of peptides.
The efficiency of peptide-display on pIII was assessed by phage ELISA. Displayed peptides were fused to FLAG-tag – pIII on the phage particle and captured by immobilized anti-FLAG antibody. After washing, the number of captured phage was assessed by anti-M13 HRP conjugate. Two positively charged peptides (Tat peptide; □ and SV40 NLS; ▨) and a neutral peptide (RGDS; ■) were used in this experiment (n = 3). Each data value represents the mean ± S.D. B) Sequences of displayed peptides and their pIs. Cationic amino acids are underlined. All pI values were calculated by Expasy Compute pI/Mw tool (http://au.expasy.org)

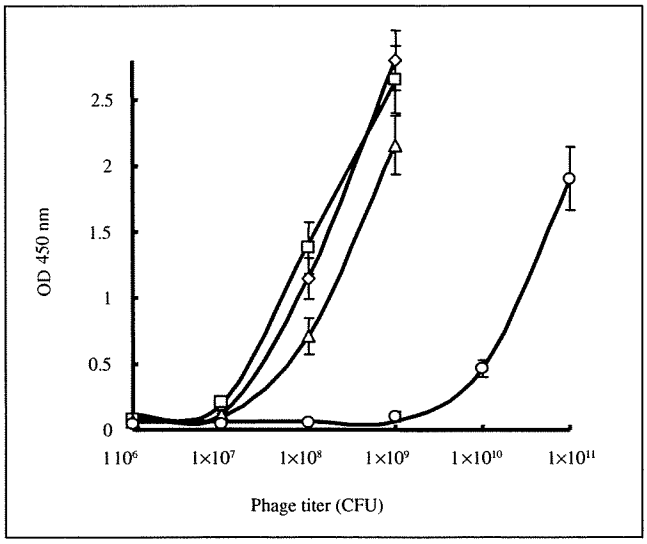

Fig. 3: Comparison of the efficiency of protein-display using pIII type phage display.
The efficiency of protein-display on pIII was assessed by phage ELISA. Proteins with different molecular weights (approximately 400–58,000 Da) were displayed on phage particle as pIII fusion proteins. This experiment was performed using the same method as Fig. 2 (n = 3). Each data value represents the mean ± S.D. □, RGDS-pIII phage; ◇, LacZ-pIII phage; △, scFv-pIII phage; ○, Importin-α-pIII phage

ated the relationship between electric charge and display efficiency using FLAG tagged ELISA (Fig. 2A). The display of positively charged SV40 NLS and HIV-1 Tat peptides were less efficient than that of the neutrally charged RGDS peptide. Generally, positively charged peptides are easy to adsorb onto various surfaces (Gaillard et al. 1999), and they repulse each other. Therefore, positively charged peptides may interfere with phage assembly in the periplasm.

Second, we examined the relationship between molecular weight and display efficiency again using FLAG tagged ELISA (Fig. 3). Because the display of positively charged sample was less efficient (Fig. 2), we used the neutrally charged proteins (pI 5.0–6.4) (MW 1.5–58 kDa) displayed on pIII to examine the influence of molecular weight on display. Phage displaying the low molecular weight RGDS peptide bound to anti-FLAG antibody at a concentration of 10^6–10^9 CFU. The higher molecular weight importin-α (58 kDa) displayed on the phage surface could not bind at the same concentration, needing 10^9–10^{11} CFU. In general, the amount of phage prepared by following the standard protocol was approximately 10^{12}–10^{13} CFU (Imai 2006). To create functional mutants using a phage library, it is desirable to use an amount of phage in excess (more than 100-fold) of the phage library (approximately 10^6–10^9 CFU). When proteins display on the phage surface efficiently, the experiment can proceed without bias. However, our result suggests that a phage library displaying high molecular weight proteins may be of low quality simply because the levels of the desired proteins are not sufficiently expressed for screening. This introduces a selection bias for those proteins that can be expressed at the proper level.

To examine the efficiency of pIII-display in greater detail, we quantified the number of molecules displayed on the phage surface by electrophoresis analysis using CsCl purified phage (Fig. 4). These results (Fig. 3, 4) demonstrate that the efficiency of RGDS peptide-display on pIII was the best (approximately 2 molecules/phage). The display efficiency decreased as the molecular weight of the target protein increased. Because the titer of all phages prepared in this experiment was determined, we suggested that the display of different molecular weight proteins did not affect the efficiency of phage-preparation (data not shown). Additionally, the proteins used in this experiment (RGDS, LacZ, scFv and importin-α) were expressed efficiently in *E. coli*. Therefore, we suggest that the efficiency with which a protein is displayed on pIII is directly related to its molecular weight.

Finally, we examined the efficiency of pVIII-display by Western blot and confirmed that it also decreased as the molecular weight increased (Fig. 5). Interestingly, this result shows that scFv (25 kDa) could be displayed on pVIII efficiently. Because the pVIII phage display system is generally believed to be limited in its application precisely by the molecular weight of displayed protein, many used it only for display of peptide libraries (Verhaert et al. 1999; Kneissel et al. 1999; Lowman 1997; Gaillard et al. 1999). However, our result suggests that the pVIII system could be applied to larger molecules. This could provide useful

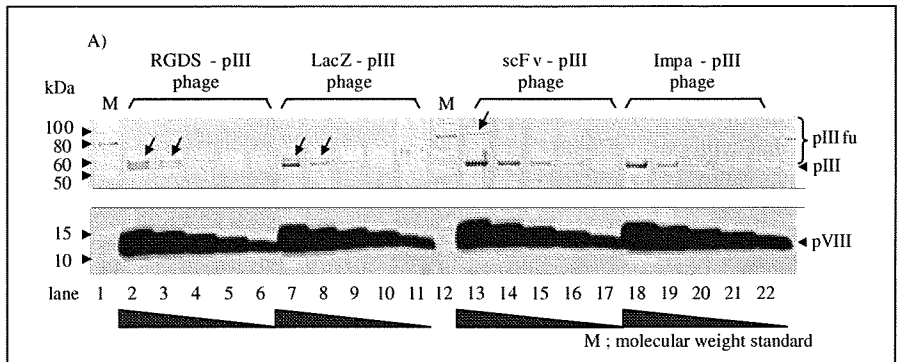

B)

	RGDS-pIII	LacZ-pIII	scFv-pIII	Impα-pIII
M.W. of displayed protein (kDa)	1.5	11	25	58
M.W. of pIII fusion protein (kDa)	52.5	62	76	109
Number of displayed proteins/phage	2.7	1.0	0.12	N.D.

N.D.; Not Detectable

Fig. 4:
Calculated quantity of pIII displayed proteins using Sypro® Ruby staining.
A) The efficiency of display on pIII was quantified using CsCl purifed phages. RGDS-pIII (lanes 2–6), LacZ-pIII (lanes 7–11), scFv-pIII (lanes 13–17) and Impα-pIII phage (lanes 18–22) were used in this experiment. Molecular weight standard was loaded in lanes 1 and 12. Starting from the left, 1×10^{13} vp, 3.3×10^{12} vp, 1.1×10^{12} vp, 3.7×10^{11} vp and 1.2×10^{11} vp were loaded. B) The number of displayed proteins per one phage particle was calculated by fluorescence image analysis. Fluorescence intensity was quantified by Typhoon image analyzer

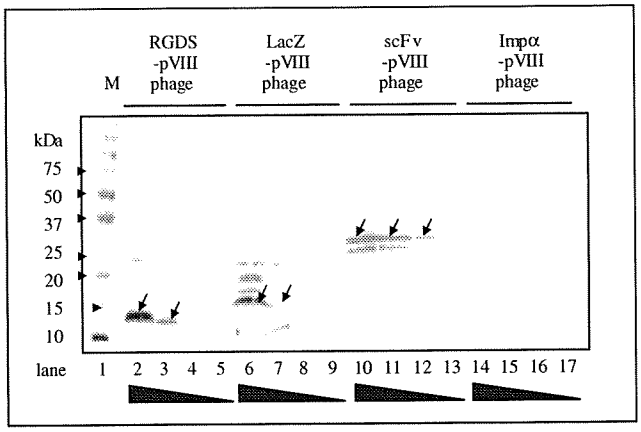

Fig. 5: Comparison of the efficiency of pVIII display protein on phage particles.
The efficiency of display on pVIII was assessed by anti-FLAG western blot. PEG-purified RGDS-pVIII (lanes 2–5), LacZ-pVIII (lanes 6–9), scFv-pVIII (lanes 10–13) and Impα-pVIII phage (lanes 14–17) were used in this experiment. Molecular weight standard was loaded in lane 1. Starting from the left, 1.5×10^{11} cfu, 5×10^{10} cfu, 1.7×10^{10} cfu and 5.5×10^{9} cfu were loaded

additional information by expanding the application of phage display systems to create various mutant proteins.
In this study, different kinds of sample peptides (SV40 NLS, HIV-1 Tat, RGDS) and proteins (RGDS, LacZ, scFv, importin-α) that could be readily expressed in *E. coli* were used as model molecules. The display of positively charged SV40 NLS and HIV-1 Tat peptides on pIII was less efficient than that of the neutrally charged RGDS peptide. When different molecular weight proteins (1.5–58 kDa) were displayed on pIII and pVIII, their display efficiencies were directly related to their molecular weights.
When comparing the efficiency of display between the four model proteins, additional factors (i.e. refolding efficiency, etc.) may account for the differences. These results show at least that the electric charge affected the efficiency of phage display and that high molecular weight proteins could not be displayed on the phage surface successfully. Recently, it was reported that improving the phagemid vector provided better efficiency of protein refolding in *E. coli* and enhanced protein display on the phage surface (Guo et al. 2003). Consequently many hope that the display efficiency of various molecules could be improved using this methodology. However, while this method improves the quality of fusion protein expression, it does not take into account the efficiency of protein assembly for the construction of phage particles. Therefore, it is still important to be able to predict the molecules that will be compatible for protein and peptide engineering using phage display by understanding the properties of this system as they were described in this report.

3. Experimental

3.1. Phagemid vectors and inserts

The pY03′-FLAG phagemid vector was modified from pCANTAB-5E (GE Healthcare Ltd.). To create this vector, the E-tag from the original vector was changed to a FLAG tag (DYKDDDDK). The pY10-FLAG phagemid vector was constructed by replacing the pIII gene in pY03′-FLAG with the pVIII gene. Genes encoding peptides (RGDS, HIV-Tat, SV40 NLS) were synthesized by Operon Biotechnologies Inc., USA. The lacZ-α gene had already been cloned into pY03′-FLAG and pY10-FLAG. The anti-KDR scFv gene was isolated from an optimized non-immune phage antibody library previously described (Imai et al. 2006). The human importin-α gene was amplified from a human bone marrow cDNA library (TAKARA Bio. Inc.). These inserts were digested and cloned into each phagemid vector.

3.2. Phage preparation

Phage was prepared by following a standard protocol. Briefly, phage particles were prepared from *Escherichia coli* (TG1 strain, Stratagene corporation) by co-infection with M13KO7 helper phage (Invitrogen Corporation). Amplified phage in culture media was roughly purified by PEG precipitation. Part of the purified phage was added to the TG1 bacteria, and the phage titer (cfu) was calculated by counting infected TG1 colonies. If necessary, additional purification using a CsCl gradient was performed as described below.

3.3. Phage ELISA

Immunoplates (Nalge Nunc International) were immobilized with anti-FLAG M2 antibody (Sigma-Aldrich Corporation) diluted to 5 μg/ml in bicarbonate buffer (Sigma-Aldrich Corporation). Plates were blocked with 2% block ace (Nakarai Tesque Inc.) for 2 h at 37 °C. Phage solution (PEG-purified) in 0.4% block ace was serially diluted and applied to the wells. After a 1 h incubation at room temperature, the binding phage was detected by anti-M13 HRP conjugate (GE Healthcare Ltd.).

3.4. Purification of phage particles under CsCl gradient

Amplified phage was purified by PEG precipitation. Phage pellets were resuspended in TBS buffer. CsCl powder (IWAI chemicals company) and additional TBS buffer were added to the phage solution up to 31%. After CsCl gradient ultracentrifugation at 400,000 × g at 5 °C for 20 h, the concentrated phage band was isolated. TBS (five volumes) was added to the purified phage and centrifuged again at 400,000 × g at 5 °C for 4 h to remove the CsCl. The obtained phage was resuspended in TBS and used for experiments.

3.5. Sypro Ruby staining

After purifying the phage under a CsCl gradient, the number of phage particles (vp/ml) was estimated from its absorbance according to the standard protocol. Serially diluted phage samples were resolved by SDS – poly acrylamide electrophoresis (SDS-PAGE). Gels were incubated in SYPRO® Ruby protein gel stain reagent (Pearce Biotechnology, Inc., USA) overnight at room temperature. After washing with wash buffer (10% methanol and 7% acetic acid) for 30 min, fluorescence was detected using the Typhoon Variable Image Analyzer (GE Healthcare Ltd.). The number of surface-displayed proteins was calculated from fluorescence intensity using ImageQuant TL software (GE Healthcare Ltd.) assuming that one phage particle contained five pIII coat proteins on its surface.

3.6. Anti-FLAG western blotting

SDS-PAGE was performed using serially diluted phage purified by PEG precipitation. Phage protein in the gel was transferred to PVDF membrane (GE Healthcare Ltd.) using the Hoefer TE 70 semi dry transfer unit (GE Healthcare Ltd.). Membranes were blocked in 4% block ace for 1 h. FLAG-tagged pVIII fusion protein was detected with anti-FLAG M2 antibody (Sigma-Aldrich Corporation) and anti-mouse IgG HRP conjugate (Sigma-Aldrich Corporation). After detection by ECL plus reagent (GE Healthcare Ltd.), its luminescence was quantitated using the LAS-3000 Lumi Imager (Fujifilm Corporation).

Acknowledgements: This study was supported in part by Grants-in-Aid for Scientific Research (No. 20015052) from the Ministry of Education, Culture, Sports, Science and Technology of Japan, by Health and Labor Sciences Research Grant from the Ministry of Health, Labor and Welfare of Japan, and in part by Research Fellowships for Young Scientists (No. 3608) from Japan Society for the Promotion of Science.

References

Bayer R, Feigenson GW (1985) Reconstitution of M13 bacteriophage coat protein. A new strategy to analyze configuration of the protein in the membrane. Biochim Biophys Acta 815: 369–379.
Chasteen L, Ayriss J, Pavlik P, Bradbury AR (2006) Eliminating helper phage from phage display. Nucleic Acids Res 34: e145.
Gaillard C, Flavin M, Woisard A, Strauss F (1999) Association of double-stranded DNA fragments into multistranded DNA structures. Biopolymers 50: 679–689.
Gourdine JP, Greenwell P, Smith-Ravin E (2005) Application of recombinant phage display antibody system in study of Codakia orbicularis gill proteins. Appl Biochem Biotechnol 125: 41–52.
Guo JQ, You SY, Li L, Zhang YZ, Huang JN, Zhang CY (2003) Construction and high-level expression of a single-chain Fv antibody fragment specific for acidic isoferritin in Escherichia coli. J Biotechnol 102: 177–189.
Imai S, Mukai Y, Nagano K, Shibata H, Sugita T, Abe Y, Nomura T, Tsutsumi Y, Kamada H, Nakagawa S, Tsunoda S (2006) Quality enhancement of the non-immune phage scFv library to isolate effective antibodies. Biol Pharm Bull 29: 1325–1330.

Keresztessy Z, Csosz E, Harsfalvi J, Csomos K, Gray J, Lightowlers RN, Lakey JH, Balajthy Z, Fesus L (2006) Phage display selection of efficient glutamine-donor substrate peptides for transglutaminase 2. Protein Sci 15: 2466–2480.

Kneissel S, Queitsch I, Petersen G, Behrsing O, Micheel B, Dubel S (1999) Epitope structures recognised by antibodies against the major coat protein (g8p) of filamentous bacteriophage fd (Inoviridae). J Mol Biol 288: 21–28.

Kuhn A (1987) Bacteriophage M13 procoat protein inserts into the plasma membrane as a loop structure. Science 238: 1413–1415.

Lowman HB (1997) Bacteriophage display and discovery of peptide leads for drug development. Annu Rev Biophys Biomol Struct 26: 401–424.

Maruta F, Parker AL, Fisher KD, Murray PG, Kerr DJ, Seymour LW (2003) Use of a phage display library to identify oligopeptides binding to the lumenal surface of polarized endothelium by ex vivo perfusion of human umbilical veins. J Drug Target 11: 53–59.

Schier R, Bye J, Apell G., McCall A, Adams GP, Malmqvist M, Weiner LM, Marks JD (1996) Isolation of high-affinity monomeric human anti-c-erbB-2 single chain Fv using affinity-driven selection. J Mol Biol 255: 28–43.

Shibata H, Yoshioka Y, Ikemizu S, Kobayashi K., Yamamoto Y, Mukai Y, Okamoto T, Taniai M, Kawamura M, Abe Y, Nakagawa S, Hayakawa T, Nagata S, Yamagata Y, Mayumi T, Kamada H, Tsutsumi Y (2004) Functionalization of tumor necrosis factor-alpha using phage display technique and PEGylation improves its antitumor therapeutic window. Clin Cancer Res 10: 8293–8300.

Sidhu SS (2001) Engineering M13 for phage display. Biomol Eng 18: 57–63.

Smith GP (1985) Filamentous fusion phage: novel expression vectors that display cloned antigens on the virion surface. Science 228: 1315–1317.

Stich N, Van Steen G, Schalkhammer T (2003) Design and peptide-based validation of phage display antibodies for proteomic biochips. Comb Chem High Throughput Screen 6: 67–78.

Takashima A, Mummert M, Kitajima T, Matsue H (2000) New technologies to prevent and treat contact hypersensitivity responses. Ann N Y Acad Sci 919: 205–213.

Verhaert RM, Van Duin J, Quax WJ (1999) Processing and functional display of the 86 kDa heterodimeric penicillin G acylase on the surface of phage fd. Biochem J 342: 415–422.

Yamamoto Y, Tsutsumi Y, Yoshioka Y, Nishibata T, Kobayashi K., Okamoto T, Mukai Y, Shimizu T, Nakagawa S, Nagata S, Mayumi T (2003) Site-specific PEGylation of a lysine-deficient TNF-alpha with full bioactivity. Nat Biotechnol 21: 546–552.

Organizer-Like Reticular Stromal Cell Layer Common to Adult Secondary Lymphoid Organs[1]

Tomoya Katakai,[2]*‡‖ Hidenori Suto,*† Manabu Sugai,*‡ Hiroyuki Gonda,*‡ Atsushi Togawa,§ Sachiko Suematsu,¶ Yukihiko Ebisuno,‖ Koko Katagiri,‖ Tatsuo Kinashi,‖ and Akira Shimizu*†‡

Mesenchymal stromal cells are crucial components of secondary lymphoid organs (SLOs). Organogenesis of SLOs involves specialized stromal cells, designated lymphoid tissue organizer (LTo) in the embryonic anlagen; in the adult, several distinct stromal lineages construct elaborate tissue architecture and regulate lymphocyte compartmentalization. The relationship between the LTo and adult stromal cells, however, remains unclear, as does the precise number of stromal cell types that constitute mature SLOs are unclear. From mouse lymph nodes, we established a VCAM-1$^+$ICAM-1$^+$MAdCAM-1$^+$ reticular cell line that can produce CXCL13 upon LTβR stimulation and support primary B cell adhesion and migration in vitro. A similar stromal population sharing many characteristics with the LTo, designated marginal reticular cells (MRCs), was found in the outer follicular region immediately underneath the subcapsular sinus of lymph nodes. Moreover, MRCs were commonly observed at particular sites in various SLOs even in Rag2$^{-/-}$ mice, but were not found in ectopic lymphoid tissues, suggesting that MRCs are a developmentally determined element. These findings lead to a comprehensive view of the stromal composition and architecture of SLOs. ***The Journal of Immunology,*** **2008, 181: 6189–6200.**

Various types of secondary lymphoid organs (SLOs),[3] situated at strategic sites throughout the body, play important roles in triggering adaptive immunity (1). Lymph nodes (LNs) and the spleen are connected with the lymphatic and blood vascular system, respectively, to filter and detect Ags in body fluids. Mucosal-associated lymphoid organizations such as Peyer's patches (PPs), nasal-associated lymphoid tissues (NALTs), isolated lymphoid follicles (ILFs), and cryptopatches (CPs) play crucial roles in mucosal surveillance. Although each SLO has a unique architecture closely associated with the surrounding anatomy, the various SLOs share some common features: for instance, the accumulated immune cell subsets are distributed into a regular pattern to form subcompartments (1). The most prominent feature of SLOs is the segregation of B and T lymphocytes. B cells form follicles (B zone) and occasionally develop germinal centers during antigenic stimulation, while the majority of T cells accumulate adjacent to the follicles (T zone) and survey cognate Ags presented by dendritic cells (DCs). Such tissue geometry is supported by mesenchymal stromal cells, which not only provide a foothold for immune cells' movement and interactions but also have the ability to regulate their homeostasis. The reticular network, composed of fibroblastic reticular cells (FRCs) and extracellular matrix (ECM) bundles, is the chief framework supporting the whole tissue architecture (2–4). Several findings have suggested that the reticular network acts as a system for transporting materials through a "conduit" consisting of ECM bundles wrapped with FRCs, (5, 6). Two distinct stromal cell types, residing in different compartments and producing specific chemokines, play key roles in the localization of lymphocytes: in the B zone, follicular dendritic cells (FDCs) expressing CXCL13 and in the T zone, FRCs expressing CCL19 and CCL21 (7–9).

Organogenesis of SLOs is considered to progress essentially through two sequential steps: first, the early formation of anlagen and, second, the maturation of tissue architecture by lymphocyte accumulation (1). LNs and PPs develop from embryonic anlagen in a similar way (10, 11), while postnatally constructed NALT and ILFs are formed through slightly different processes (12, 13). Organogenesis of the spleen is more complicated because it consists of distinct tissues, a lymphoid compartment (white pulp) and the red pulp (14). The initial key event in LN and PP organogenesis is the intimate interaction between hematopoietic CD45$^+$CD4$^+$ CD3$^-$ lymphoid tissue "inducer" (LTi) cells and specialized mesenchymal "organizer" (LTo) cells expressing VCAM-1, ICAM-1, and mucosal addressin cell adhesion molecule 1 (MAdCAM-1) (15–18). LTi cells express lymphotoxin (LT) $\alpha1\beta2$, which transmits signals through lymphotoxin β receptor (LTβR) on LTo cells, leading to the activation of NF-κB transcription factor complexes, not only RelA/p50 (canonical pathway) but also RelB/p52 (noncanonical pathway) via NF-κB-inducing kinase (NIK) (11, 19). In LTo cells, this cascade up-regulates VCAM-1, ICAM-1, MAdCAM-1, and homeostatic chemokines, driving a positive

*Center for Genomic Medicine, Graduate School of Medicine and †Graduate School of Biostudies, Kyoto University and ‡Translational Research Center, Kyoto University Hospital, Kyoto, Japan; §Laboratory for Stem Cell Biology, RIKEN Center for Developmental Biology, Kobe, Japan; ¶Laboratory of Immune Cell Regulation, National Institute of Biomedical Innovation, Ibaraki; and ‖Department of Molecular Genetics, Institute of Biomedical Science, Kansai Medical University, Moriguchi, Japan

Received for publication July 8, 2008. Accepted for publication September 3, 2008.

The costs of publication of this article were defrayed in part by the payment of page charges. This article must therefore be hereby marked *advertisement* in accordance with 18 U.S.C. Section 1734 solely to indicate this fact.

[1] This work was supported in part by Grants-In-Aid for Science Research on Priority Areas from the Ministry of Education, Culture, Sports, Science and Technology of Japan.

[2] Address correspondence and reprint requests to Dr. Tomoya Katakai, Department of Molecular Genetics, Institute of Biomedical Science, Kansai Medical University, Moriguchi 570-8506, Japan. E-mail address: katakait@takii.kmu.ac.jp

[3] Abbreviations used in this paper: SLO, secondary lymphoid organ; CP, cryptopatch; ECM, extracellular matrix; FAE, follicle-associated epithelium; DC, dendritic cell; FDC, follicular DC; FRC, fibroblastic reticular cell; LT, lymphotoxin; LTi/o, lymphoid tissue inducer/organizer; MRC, marginal reticular cell; NALT, nasal-associated lymphoid tissue; PP, Peyer's patch; SCS, subcapsular sinus; LN, lymph node; NIK, NF-κB-inducing kinase; ILF, isolated lymphoid follicle; TRANCE, TNF-related activation-induced cytokine; DAPI, 4,6-diamidino-2-phenylindole; PTx, pertussis toxin; MAdCAM-1, mucosal addressin cell adhesion molecule 1; FAE, follicle-associated epithelium.

feedback loop by further attracting LTi cells. Mice lacking the above signaling components exhibit various degrees of SLO deficiency and malformation (19). Generation of LTi cells from fetal liver progenitor involves Id2 and RORγt; mice deficient in these gene products show a complete loss of LTi cells and lack all LNs and PPs (20–22). TNF-related activation-induced cytokine (TRANCE), a key factor in osteoclastogenesis, participates in the proliferation and differentiation of LTi cells, particularly in the LN anlagen (23); hence, all LNs but not all PPs are absent in mice deficient in TRANCE or its receptor TRANCE-R (24, 25). Conversely, IL-7Rα expressed on LTi cells and its downstream signaling pathway are essential for the development of PPs but not LNs (16, 26). Formation of splenic white pulp does not require LTi cells, but the maturation of the tissue structure depends on LTα1β2 produced by lymphocytes and LTβR signaling (14). Therefore, despite some similarities, the developmental program and molecular requirements of each SLO are clearly different.

Even after the maturation of SLOs, continuous interplay between lymphocytes and stromal cells is likely to be required for the maintenance of tissue architecture and characteristics of adult stromal cells. Despite their importance in the spatiotemporal regulation of immune cell behavior, however, only limited information about the cytological nature of adult stromal cells has been obtained so far. It remains unknown how many different mesenchymal stromal cell types exist in particular SLOs. The relationship between embryonic LTo cells and such different types of stromal cells in adult SLOs, i.e., the postnatal fate of LTo cells, is also unclear. It is possible that LTo-like cells might still exist in the adult and play some role in the maintenance of SLOs. Since variations in stromal cells might account for the differences in both developmental program and local immune responses, it is important to clarify the common features and differences between the various SLOs.

In this study, we report the detailed characterization of a reticular stromal cell line derived from adult mouse LN, which can produce CXCL13 upon LTβR signaling. We also found a layer of unique reticular cells underneath the subcapsular sinus lining of the LNs. These specialized mesenchymal cells share many characteristics with LTo cells and are commonly observed at certain places in various types of adult SLOs. Taken together, our observations provide new insights into the development and tissue organization of SLOs.

Materials and Methods

Mice

Mice were maintained at the animal facility in the Center for Genomic Medicine (Kyoto University). *aly/aly* mice were purchased from CLEA Japan. Experimental procedures involving animals were approved by the Animal Research Committee, Graduate School of Medicine, Kyoto University and conducted according to the guidelines for animal treatment of the Institute of Laboratory Animals (Kyoto University).

Cells

BLS4 and BLS12 cells were established from peripheral LNs of BALB/c mouse as described previously (4). Cells were maintained in DMEM supplemented with 100 U/ml penicillin, 100 μg/ml streptomycin, and 10% FCS. For ECM network formation, confluent BLS12 cells grown on 8-well chamber slides (Nalgen Nunc International) were cocultured with 2×10^6 LN cells for 6 days and examined for matrix production. Stable transfectants overexpressing human NIK were made using a retrovirus vector system (4). Primary B and T cells were isolated from spleen and LNs using a MACS B or T cell isolation kit (Miltenyi Biotec).

Abs and reagents

Primary Abs used for immunohistochemistry or flow cytometry were as follows: as primary reagents, ER-TR7 (BMA), FITC-anti-B220 (RA3-6B2), anti-CR1 (8C12) (BD Pharmingen), anti-MAdCAM-1 (MECA-367; Serotec), biotin-anti-CXCL13 (BAF470), biotin-anti-VCAM-1 (BAF643), anti-LYVE-1 (AF2125), anti-LTβR (AF1008; R&D Systems), anti-VCAM-1 (MK2; Immunotech), biotin-anti-CD3ε (145-2C11), PE-anti-CD4 (GK1.5), anti-ICAM-1 (YN1/1.7.4), anti-PDGFRβ (APB5), anti-TRANCE (IK22/5; eBioscience), anti-fibronectin (H-300), anti-RelB (C-19; Santa Cruz Biotechnology), anti-laminin (LSL), anti-podoplanin/gp38 (HG-19), FITC-peanut agglutinin (PNA; Sigma-Aldrich), anti-FcγRII/III (2.4G2), anti-CD44 (KM201), anti-gp38 (8.1.1; Ref. 27), anti-FDC-M2 (209; Ref. 28), and biotin-anti-BP-3 Ab (29) (hybridoma supernatants or purified Abs); as secondary reagents, PE-anti-rat IgG, allophycocyanin-anti-rat IgG, biotin-anti-rat IgG, FITC-anti-hamster IgG (Caltag Laboratories), FITC-anti-rabbit IgG, Cy5-anti-rabbit IgG (The Jackson Laboratory), Alexa Fluor 488-anti-rabbit IgG, Alexa Fluor 488-anti-goat IgG, PE-streptavidin, and allophycocyanin-streptavidin (Molecular Probes). Abs against integrin α_L (KBA2) and α_4 (PS/2) were purified from hybridoma supernatants.

Immunohistochemistry

Tissues isolated from animals were embedded in OTC compound (Sakura Finetechnical) and then frozen in liquid nitrogen. Frozen sections (10-μm thick) were fixed with cold acetone. BLS12 cells plated on chamber slides (Nalgen Nunc International) with or without coculturing or factor treatment were fixed with 3% paraformaldehyde-PBS and then permeabilized with 0.2% Triton X-100. After blocking with 1% BSA/0.05% Tween 20-PBS, sections or cells were stained with Abs. Nuclear DNA was stained with 4,6′-diamidino-2-phenylindole (DAPI; Sigma-Aldrich). Sections or cells were examined using a confocal laser scanning microscope (TSC-SP2; Leica). Digital images obtained were prepared using Adobe Photoshop software (Adobe Systems).

Flow cytometry

BLS12 cells were harvested from culture dishes using 0.02% EDTA-PBS. After blocking with PBS containing 1% BSA, the cells were stained with Abs by direct or indirect methods, counted using a FACSCalibur flow cytometer (BD Biosciences), and analyzed using CellQuest software (BD Biosciences).

ELISA

Confluent BLS12 cells in 24-well culture plates were stimulated with mouse TNF-α (10 ng/ml; PeproTech), human TNF-β (LTα3, 10 ng/ml; PeproTech), and/or polyclonal goat anti-mouse LTβR Ab (0.5 μg/ml; R&D Systems). Production of CXCL13 and CCL19 in culture supernatants was detected by sandwich ELISA using DuoSet (R&D Systems) according to the manufacturer's recommendations.

RT-PCR analysis

RT-PCR analysis was performed as described previously (30). Specific primer pairs used in this study were as follows: GAPDH, 5′-CCATCA CCATCTTCCAGGAG-3′ and 5′-CCTGCTTCACCACCTTCTTG-3′; CXCL13, 5′-TTGAACTCCACCTCCAGGCA-3′ and 5′-CTTCAGGCAG CTCTTCTCTT-3′; CCL5, 5′-TCTGAGACAGCACATGCATC-3′ and 5′-CCTAGCTCATCTCCAAATAG-3′; CCL19, 5′-GCACACAGTCTCTCA GGCTC-3′ and 5′-CTCTCTTCTGGTCCTTGGTT-3′; CCL21, 5′-AGCT ATGTGCAAACCCTGAG-3′ and 5′-TCATAGGTGCAAGGACAAGG-3′; CXCL12, 5′-AAACCAGTCAGCCTGAGCTAC-3′ and 5′-TTACTTG TTTAAAGCTTTCTC-3′; IL-7, 5′-TCCTCCACTGATCCTTGTTC-3′ and 5′-TTGTGTGCCTTGTGATACTG-3′; and BAFF, 5′-TCGTGGAAT GGATGAGTCTG-3′ and 5′-TCTGTTTCCTCTGGTCCCTG-3′.

Lymphocyte adhesion to BLS12

The in vitro adhesion assay was performed as described previously, with slight modifications (31). BLS12 cells were plated on fibronectin-coated (20 μg/ml) 96-well plates and cultured for 2–3 days to form monolayers. Twenty-four hours before the assay, the confluent BLS12 monolayer was stimulated with agonistic anti-LTβR Ab (0.5 μg/ml). Primary lymphocytes were labeled with 1 μg/ml 2′,7′-bis-(2-carboxyethyl)-5-(and-6)-carboxyfluorescein (Molecular Probes) at 37°C for 20 min. Labeled lymphocytes were applied to the BLS12 monolayer at 5×10^5 cells/well and incubated at 37°C for 30 min with or without 20 μg/ml blocking Abs. Alternatively, lymphocytes were pretreated with 0.2 μg/ml pertussis toxin (PTx) or B oligomer (Calbiochem) at 37°C for 2 h. Nonadherent cells were removed by five consecutive washes. Input and bound cells were measured using a fluorescence multiwell plate reader (Cytofluor4000; Applied Biosystems).

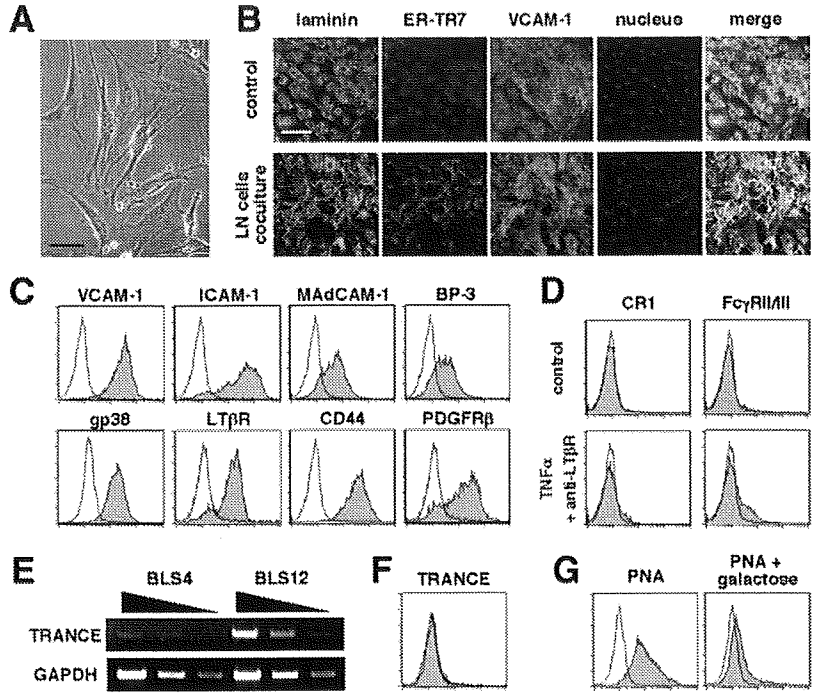

FIGURE 1. Basic characterization of adult LN stromal cell line BLS12. *A*, BLS12 cells show fibroblastic morphology. A phase-contrast view of growing cells on plastic dishes is shown. Bar, 50 μm. *B*, BLS12 produces reticular matrix via contact with lymphocytes. BLS12 monolayers on chamber slides were cocultured with LN cells for 6 days. After fixation and permeabilization, cells were stained with Abs against laminin, ER-TR7, and VCAM-1, counterstained with DAPI, and examined by confocal microscopy. Bar, 100 μm. *C*, Cell surface markers expressed on BLS12 cells. EDTA-harvested BLS12 cells were stained for the indicated surface markers and analyzed by flow cytometry. Histograms show overlays of stained (filled histograms) and control (open histograms). *D*, No significant expression of CR1 or FcγRII/III is induced in BLS12 by dual signaling through TNFR and LTβR. Cells were stimulated with or without TNF-α (10 ng/ml) and agonistic anti-LTβR Ab (0.5 μg/ml) for 2 days. Harvested cells were stained for CR1 and FcγRII/III and analyzed by flow cytometry. *E* and *F*, BLS12 constitutively expresses TRANCE mRNA, but TRANCE protein is undetectable at the cell surface. The transcript for TRANCE was detected by RT-PCR (*E*). The amounts of PCR products amplified from 5-fold serial dilutions of BLS12 cDNAs were standardized relative to GAPDH. Another reticular cell line, BLS4, was used as a control and showed little expression of TRANCE mRNA. Cell surface TRANCE protein was analyzed by flow cytometry (*F*). *G*, BLS12 displays carbohydrates recognized by PNA. Cells were stained with FITC-PNA in the presence or absence of 0.2 M galactose and analyzed by flow cytometry. Addition of galactose markedly diminishes the PNA binding to BLS12 cells, indicating that most of the binding is mediated by the lectin activity of PNA.

B cell migration on BLS12 monolayer

BLS12 cells were seeded on fibronectin-coated (20 μg/ml) ΔT dish (Bioptechs) and cultured for at least 5 days to construct a monolayer. The confluent BLS12 monolayer was stimulated with agonistic anti-LTβR Ab (0.5 μg/ml) for 24 h. Primary B cells (5×10^5) were loaded onto activated BLS12 monolayers in RPMI 1640 medium supplemented with 8% FCS and 10 mM HEPES. After 3 h of incubation, phase-contrast images were obtained every 30 s for 30 min at 37°C on a LSM510 confocal laser microscope (Zeiss) equipped with a heating stage system for ΔT dishes (Bioptechs). Blocking Abs (final concentration, 20 μg/ml) were added 30–60 min before commencement of image capture. Alternatively, lymphocytes were pretreated with 0.2 μg/ml PTx or B oligomer (Calbiochem) at 37°C for 2 h. Image data were analyzed using Image-Pro Plus software (Media Cybernetics). In each field, 40–50 randomly selected cells were manually tracked to measure mean velocity and displacement from starting point.

Fc chimeric proteins

LTβR-Fc and Il-6 TCRVα-Fc chimeric proteins were produced as described previously (26, 30). Specifically, X63.653 myeloma cells were stably transfected with each vector construct, and chimeric proteins were purified from culture supernatants or ascites fluid using a protein G- Sepharose column (Amersham Biosciences). Mice were i.v. injected weekly with 100–200 μg of chimeric proteins and were sacrificed 2–4 wk later to obtain SLOs.

Results

Stromal cell line BLS12 is reticular fibroblast with the ability to produce CXCL13 upon LTβR-NIK signaling

We previously established a series of stromal cell lines from adult mice LNs (4). One of these, BLS12, showed typical fibroblastic morphology (Fig. 1*A*). When cocultured with lymphocytes, BLS12 showed the ability to produce ECM meshwork that contains laminin, fibronectin, and ER-TR7-Ag (Fig. 1*B* and data not shown), indicating that this cell line preserves FRC features. It is worth noting that BLS12 constitutively expressed MAdCAM-1 and BP-3 (CD157), in addition to FRC markers such as VCAM-1, ICAM-1, and gp38 (podoplanin) on the surface (Fig. 1*C*). BLS12 also expressed LTβR, CD44, and a mesenchymal marker, PDGFRβ (Fig. 1*C*). In contrast, FDC markers CR1 (CD35) and FcγRII/III (CD16/32) were undetectable, and were virtually uninducible even when the cells were simultaneously stimulated with TNF-α and agonistic anti-LTβR Ab (Fig. 1*D*) or cocultured with lymphocytes (data not shown). Although surface expression of TRANCE protein was undetectable in BLS12, the mRNA was readily detected, in contrast to another FRC line, BLS4, in which TRANCE mRNA was almost undetectable (Fig. 1, *E* and *F*). In addition, BLS12 cells displayed cell surface carbohydrates recognized by PNA (Fig. 1*G*).

Of prime importance, BLS12 cells exhibited the ability to express CXCL13 upon LTβR ligation and a substantial amount of CXCL13 protein was detected in the culture supernatant (Fig. 2, *A* and *B*). Although TNFR ligands, TNF-α or LTα3, did not induce CXCL13 on their own, both of these cytokines markedly augmented the LTβR-induced CXCL13 expression. The stable overexpression of NIK in BLS12 cells resulted in spontaneous CXCL13 production (Fig. 2, *C* and *D*), suggesting that excessive NIK is sufficient for inducing CXCL13 in this cell context. We

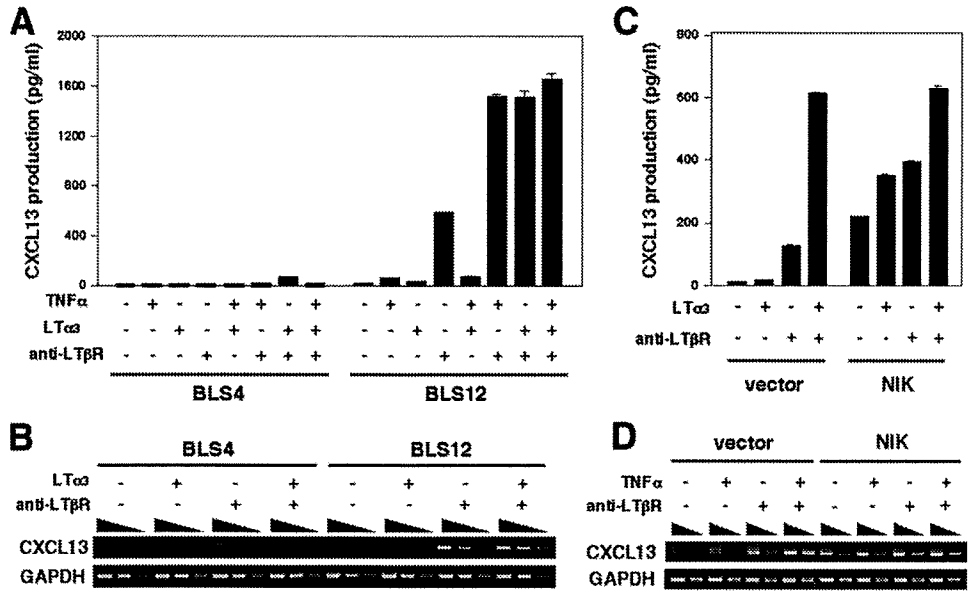

FIGURE 2. BLS12 produces CXCL13 upon LTβR-NIK signaling. *A* and *B*, BLS12 but not BLS4 produces CXCL13 in response to LTβR ligation. BLS cells were stimulated with TNF-α, LTα3, anti-LTβR Ab, or combinations of these stimulants for 5 days. CXCL13 protein in the supernatant was measured by ELISA (*A*). The results are shown as means ± SD. Note that TNF-α and LTα3 used in our experiments exert almost equivalent enhancing effects on LTβR-mediated CXCL13 production. The transcript for CXCL13 was detected by semiquantitative RT-PCR analysis 2 days after the stimulation (*B*). *C* and *D*, Overexpression of NIK induces spontaneous CXCL13 production in BLS12. BLS12 stably transfected with control (vector) or NIK was stimulated with LTα3 (or TNF-α), anti-LTβR Ab, or combinations thereof for 2 days. CXCL13 expression was analyzed by ELISA (*C*) and RT-PCR (*D*).

also detected CCL19 mRNA only when BLS12 cells were simultaneously stimulated with LTα3 (or TNF-α) and agonistic anti-LTβR Ab (Fig. 3); however, the secreted protein level was nearly undetectable (data not shown). In contrast, no CCL21 expression could be detected irrespective of the presence or absence of any stimuli tested (data not shown). BLS12 cells also expressed factors required for lymphoid homeostasis, such as IL-7, BAFF, and CXCL12 (Fig. 3).

BLS12 supports the motility of primary B cells

To investigate the interaction between lymphocytes and BLS12, we first examined the adhesion of B cells to BLS12 cells. Approximately 20% of freshly isolated B cells adhered to an unstimulated BLS12 monolayer after several hours of incubation; this adhesion was much more effective than to BLS4 monolayer, which bind only below 5% of primary B cells (Fig. 4*A*). Prestimulation of BLS12 cells with agonistic anti-LTβR Ab slightly augmented the adhesion. The adhesion of B cells to BLS12 cells was markedly inhibited by anti-α_4 integrin Ab and weakly inhibited by anti-α_L integrin Ab (Fig. 4*B*). The mixture of the two Abs blocked almost all of the adhesion. The pretreatment of B cells with PTx also dramatically inhibited the adhesion, while B oligomer, the noncatalytic subunit of PTx, showed virtually no effect (Fig. 4*C*). Taken together, these data indicate that Gαi-dependent signaling and integrins mediate B cell adhesion to BLS12 in this experimental setting.

We next addressed whether primary B cells are motile on the surface of BLS12. For this purpose, B cells were loaded onto a monolayer of LTβR-stimulated BLS12 and incubated for several hours in a heating chamber system. Under such conditions, time-lapse image analysis revealed that the B cells actively migrated on BLS12, showing significant displacement from the starting point with an average velocity of 5–6 μm/min (Fig. 4, *D–F*, and video 1[4]). Addition of Abs against integrins (Fig. 4, *D–F*, and videos 2 and 3) or pretreatment of B cells with PTx (Fig. 4, *G–I*, and videos 4 and 5) significantly reduced both velocity and displacement, suggesting that the motility of B cells on BLS12 is partially mediated by Gαi-dependent signaling and integrins, while residual motile activity is driven by unknown cues. Taken together, the data demonstrate that BLS12 has the unique property of supporting the motility of B cells.

Marginal reticular cell (MRC) layer is a unique stromal network in adult LNs

From the aforementioned results, we noticed that BLS12 cells share some characteristics with FDCs, e.g., the expression of MAdCAM-1 and BP-3, LTβR-dependent CXCL13 production, and the capacity to support B cell behavior. However, these cells express neither CR1 nor FcγRII/III, both of which are crucial and functional markers of FDCs (32). In addition, FDCs are generally weak producers of reticular fibers (3). These facts prevent us from considering BLS12 to be a FDC line.

To obtain a clue about the origin of BLS12, we examined in detail the stromal structure of the LNs. As has been well established, the FDC network was clearly observed at the center of the follicles, which

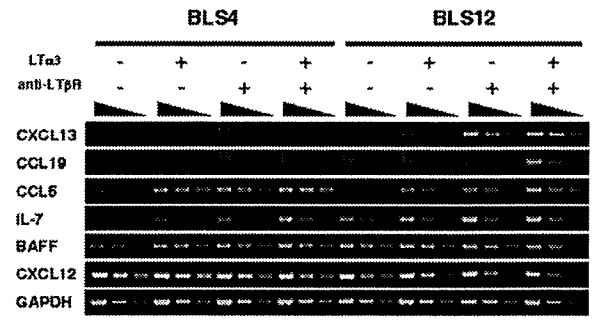

FIGURE 3. BLS12 cells express some lymphoid homeostatic factors. BLS4 and BLS12 cells were stimulated with LTα3, anti-LTβR Ab, or combinations thereof for 2 days. Transcripts for the indicated factors were detected by RT-PCR. The amounts of PCR products amplified from 5-fold serial dilutions of cDNAs were standardized relative to GAPDH.

[4] The online version of this article contains supplemental material.

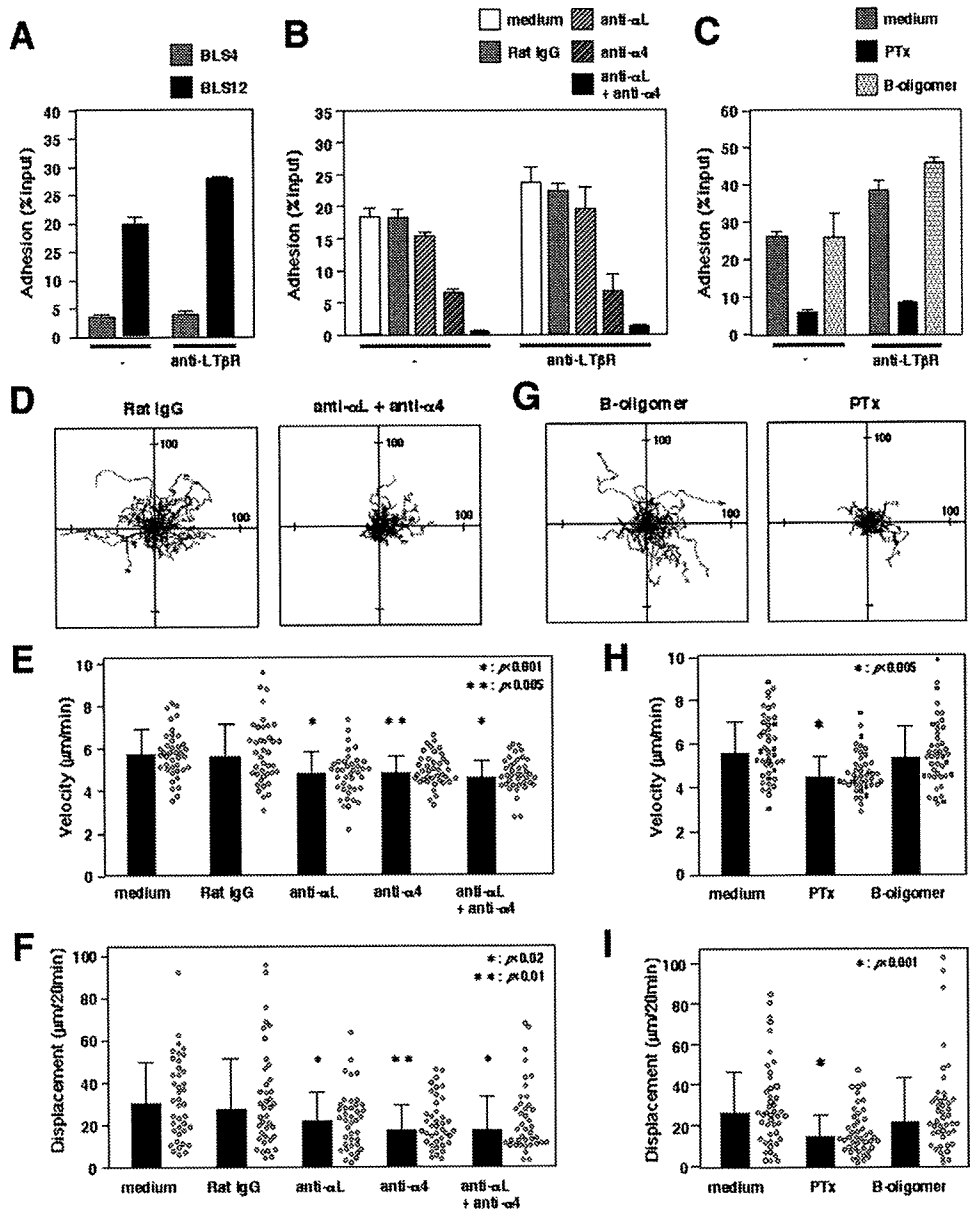

FIGURE 4. BLS12 supports the migration of primary B cells. *A*, Primary B cells adhere to BLS12. Adhesion of fluorescence-labeled B cells to BLS12 or BLS4 monolayer after 3 h of incubation was measured. Results are shown as means ± SD. *B*, The adhesion of B cells to BLS12 is integrin dependent. B cell adhesion to BLS12 in the presence or absence of Abs (20 μg/ml) was measured. *C*, Gαi-dependent adhesion of B cells to BLS12. B cells were pretreated with PTx or B oligomer and adhesion to BLS12 was measured. *D–F*, BLS12 supports the motility of B cells, which is partially inhibited by Abs against integrins. *D*, Trajectory of B cells with control IgG (*left*) or anti-integrin Abs (*right*). Each line represents a single cell's track over a 20-min time span recorded. Units are in micrometers. *E* and *F*, Anti-integrin Abs partially inhibit the motility of B cells. Each dot represents the average velocity (*E*) and displacement (*F*) of single cells. Columns represent medians ± SD of the population and asterisks indicate significantly different from control rat IgG. *G–I*, Pretreatment of B cells with PTx but not B oligomer partially inhibits the motility on BLS12. *G*, Trajectory of B cells pretreated with B oligomer (*left*) or PTx (*right*). Asterisks indicate significant differences from control.

highly expressed CR1, MAdCAM-1, BP-3, and CXCL13, as well as VCAM-1, ICAM-1, and gp38 (Fig. 5*A*). The nuclear accumulation of RelB in this region was also evident (Fig. 5*Ad*). All of the markers overlapped well in the follicular center. During the course of careful examinations, we found that there was a notable stromal cell layer at the outer margin of the cortex, i.e., the lining of the subcapsular sinus (SCS). This cell layer was brightly positive for MAdCAM-1, CXCL13, BP-3, VCAM-1, ICAM-1, and gp38, but not present in paracortical and medullary sinuses (Fig. 5*A*, red arrows). At most, a faint expression of CR1 was detected in this region. Stromal cells in this restricted area strongly expressed TRANCE, in contrast with the FDC network, which was barely stained for TRANCE (Fig. 5*Af*). Higher magnification views revealed that the layer is composed of a kind of reticular cell network (Figs. 5*B*), which extends several 10s of micrometers from the abluminal side of the SCS immediately underneath the layer of LYVE-1$^+$ lymphatic endothelial cells and the basement membrane-like ECM "floor," indicated by laminin and ER-TR7 (Fig. 5*C*). CXCL13 was detected in a filamentous pattern concurrent with the network (Fig. 5*Ba*). Nuclear RelB accumulation and PNA binding were also evident in this stromal layer (Fig. 5*Ad* and data not shown). Taking these observations together, we concluded that this specialized type of reticular cells represents a distinct population from stromal cells in the other regions, including FDCs and T zone FRCs, and hence designated these cells the MRCs (Fig. 5*D*).

MRC layer is a stromal structure common to different types of SLOs

It is well known that MAdCAM-1$^+$ FRCs, termed the marginal sinus-lining cells, encircle the inner lymphoid sheath of the splenic white pulp (Fig. 6*A*). This stromal layer expressed almost the same marker set with MRC in LNs, including CXCL13, TRANCE, BP-3, gp38, RelB, PNA-binding carbohydrates, laminin, and ER-TR7 (Fig. 6*A* and data not shown), suggesting that reticular cells aligned in this region are equivalent to LN MRCs. The layer was more obvious in the outer margin of the follicles (Fig. 6*A*, arrows) than in the interfollicular channel region (Fig. 6*A*, asterisks). MRC-like stromal networks were also observed in mucosal SLOs such as PPs, NALTs, ILFs (Fig. 6, *B–D*), and cecal lymph patches (data not shown). In all cases, MRC-like cells constituted reticular

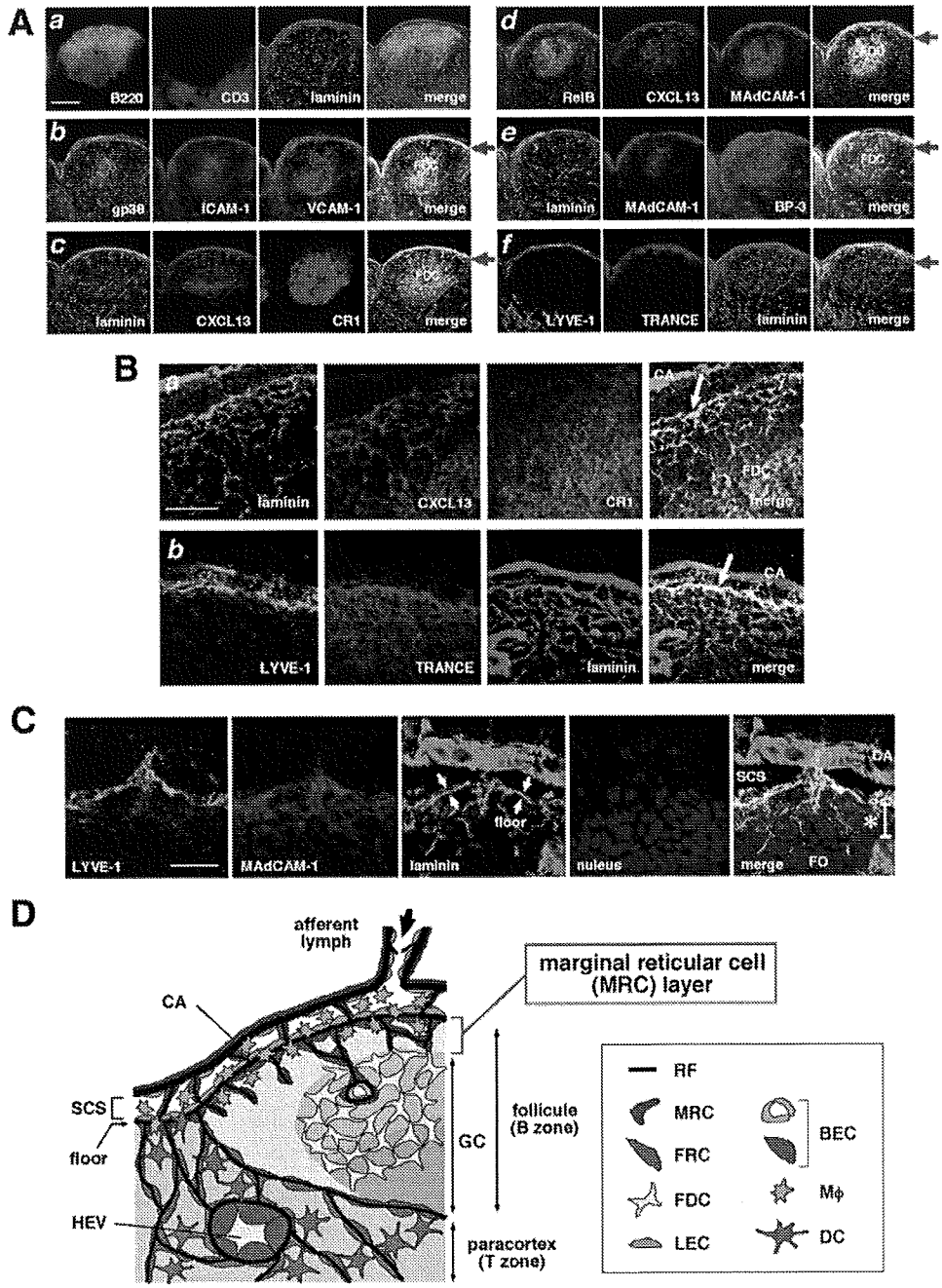

FIGURE 5. A unique reticular stromal layer in the outer margin of adult LN. *A*, Stromal markers are highly expressed in the subcapsular region of LNs. Sections of LNs were stained for various markers and examined by confocal microscopy. Outer cortical regions of the LNs are shown. Red arrows indicate SCS lining. Note that the network of FDCs is present in the center of follicles with high expression of all markers other than TRANCE. Bar, 200 μm. *B* and *C*, Specialized stromal cells constitute the reticular network underneath SCS (arrows in *B* and an asterisk in *C*). Higher magnification views of the subcapsular regions of LNs are shown. Arrows in *C* indicate basement membrane-like floor in the SCS lining. Bars, 50 μm in *B* and 20 μm in *C*. *D*, Schematic representation of MRC layer and the cortical stromal structure of the LNs. Various stromal cells of mesenchymal, endothelial, and myeroid origins, as well as matrix components are included, while lymphocytes are omitted for simplification. The MRC layer is located at the cortical side of the SCS lining, underneath the single layer of lymphatic endothelial cells that covers the luminal surface of the SCS. BEC, Blood endothelial cell; CA, capsule; FO, follicle; GC, germinal center; HEV, high endothelial venule; LEC, lymphatic endothelial cell; Mϕ, macrophage; RF, reticular fiber.

layers restricted to the subepithelial dome region immediately beneath the follicle-associated epithelium (FAE; Fig. 6*E*). In contrast, a MRC-like population was not found in ectopic lymphoid tissues in the stomach induced in mouse models for gastric autoimmunity (30, 33) (data not shown). These data indicate that the MRC layer is a common stromal structure in SLOs.

LTo cells in the marginal area of LN anlagen expand to form the MRC layer during postnatal development

Given that MRCs and LTo stromal cells share many markers, we speculated that there is some relationship between the two mesenchymal lineages. To address this issue, we examined the transitional process of stromal architecture from anlagen to postnatally developing SLOs. A structural examination of fetal LN anlagen has already been reported (34) and the authors showed that ICAM-1^{high}VCAM-^{high}MAdCAM-1^{high} (IVM^{high}) LTo cells expressing chemokines and TRANCE are concentrated in the outer region of the anlagen surrounded by LYVE-1^+ lymphatic vasculature, while IVM^{low} cells are localized in deeper regions. We confirmed similar histology of LNs on the day of birth, at which time the LNs still retain the characteristics of anlagen, as few lymphocytes have yet migrated (Fig. 7*A*). $CD4^+CD3^-$ LTi cells accumulated in the outer region of anlagen adjacent to presumptive SCS, where stromal cells highly expressing VCAM-1 and ICAM-1 formed a dense layer (Fig. 7*A*, *a* and *b*). In addition to blood vessels, these LTo also expressed MAdCAM-1 (Fig. 7*Ac*). Although TRANCE staining illuminated the whole anlage, a group of stromal cells with higher TRANCE expression clearly delineated the boundary of the lymphatic sinus (Fig. 7*Ad*). A faint signal for CXCL13 was detected in the same cells (Fig. 7*Ac*). Overall, the LN anlagen seem to be segregated into roughly outer and inner parts during ontogeny, and the stromal cells in the former exhibit a phenotype typical of LTo.

At day 6, the size of LNs markedly increased as the influx of lymphocytes and their compartmentalization in the cortical area

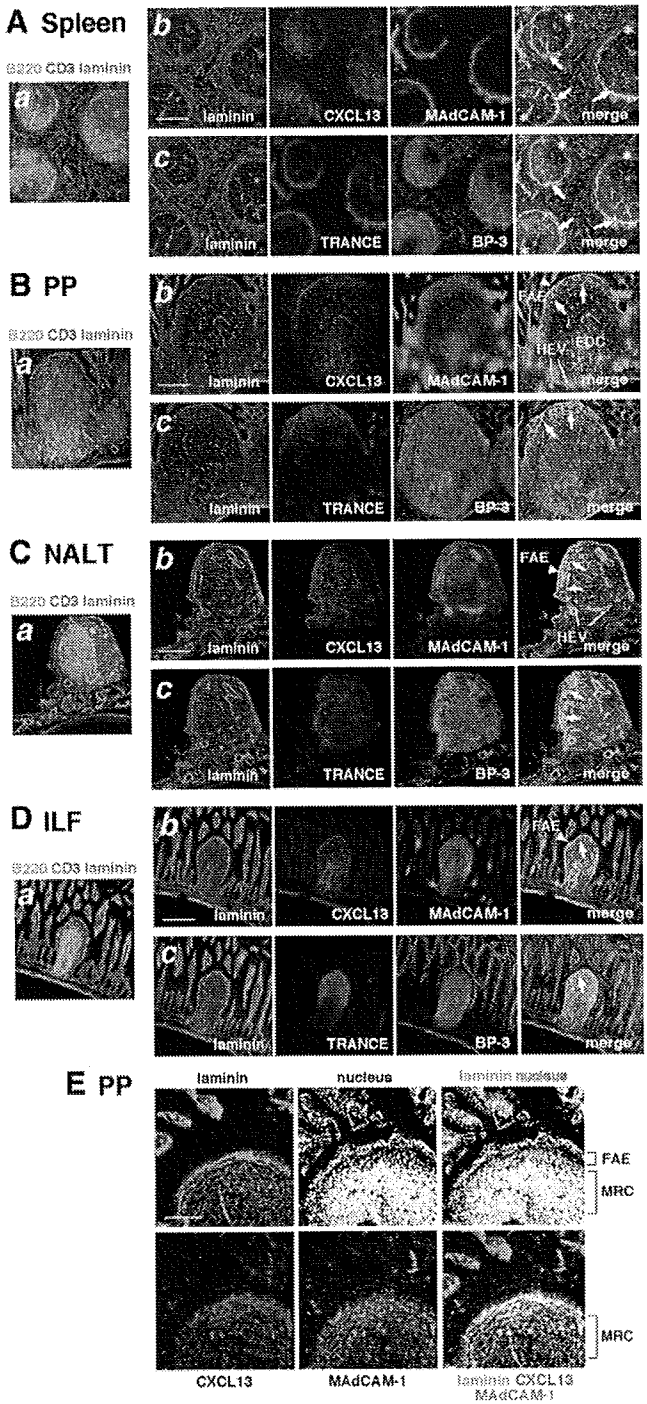

FIGURE 6. MRC layers are present in particular regions of various SLOs. *A*, Reticular stromal cells in the marginal sinus lining of splenic white pulp show characteristics of MRCs. Serial sections of spleen were stained for various markers and examined by confocal microscopy. A composite image of a section stained for laminin, CD3, and B220 shows tissue architecture and lymphocyte localization (*a*). Well-known MAdCAM-1$^+$ marginal sinus-lining cells highly express the set of MRC markers (arrows). The MRC-like layer is obscure in the interfollicular channel region (asterisks). *B–D*, Reticular stromal cells in the subepithelial dome of PP (*B*), NALT (*C*), and ILF (*D*) show characteristics of MRCs (arrows). Arrowheads indicate FAE. Luminal surface of the epithelia is often nonspecifically stained by anti-CXCL13 Ab. Higher expression of MAdCAM-1 is observed in FDCs and high epithelial venules. Bars, 200 μm. *E*, Higher magnification view of the subepithelial dome region in the PP. Section was stained with Abs against laminin, CXCL13, and MAdCAM-1 and counterstained with DAPI for the visualization of the nucleus. MRC network is localized immediately underneath the FAE layer (laminin$^-$ CXCL13$^-$MAdCAM-1$^-$). Bar, 100 μm.

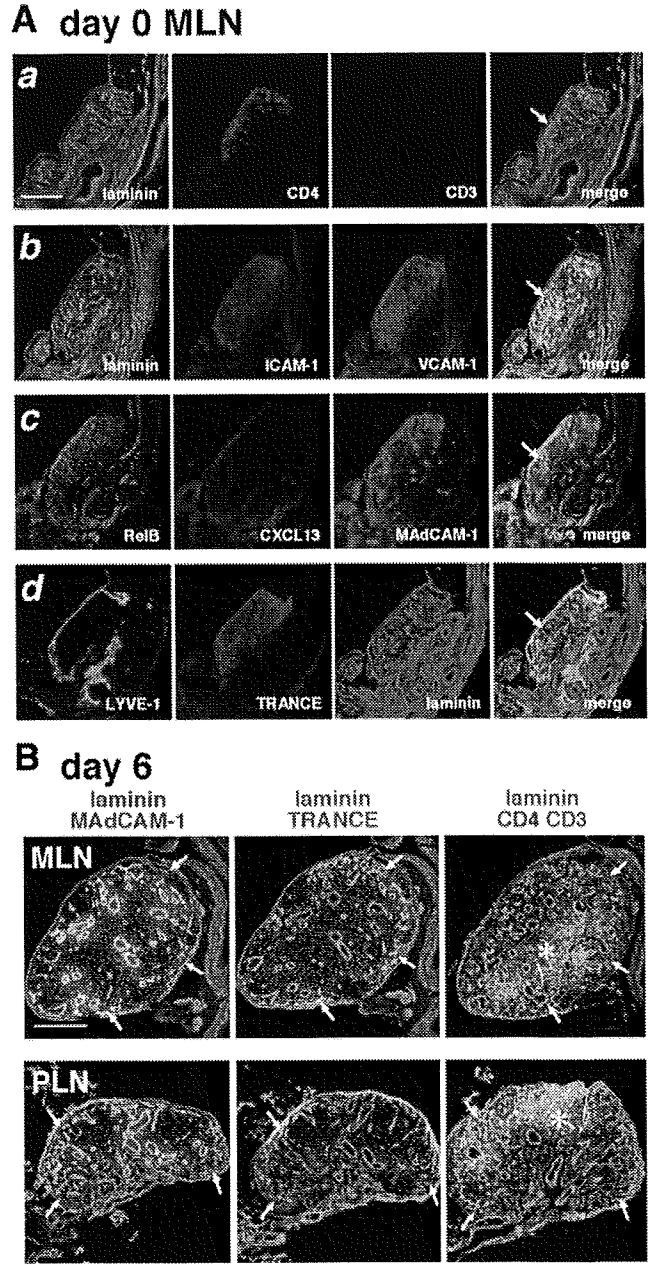

FIGURE 7. Continuity between LTo stroma and MRC layer during postnatal development of LNs. *A*, Stromal architecture of day 0 mesenteric LNs (MLN). Serial sections of mesentery, including mesenteric LNs from day 0 mouse, were stained for the indicated markers. CD4$^+$CD3$^-$ LTi cells (*a*) are accumulated in the marginal region of the anlagen, where LTo stromal cells with higher expression of ICAM-1, VCAM-1 (*b*), MAdCAM-1 (*c*), and TRANCE (*d*) are condensed underneath presumptive SCS (arrows). Bar, 200 μm. *B*, Expansion of the MRC layer in postnatally growing LNs. Composite images of day 6 mesenteric LNs and peripheral LNs (PLN) are shown. Presumptive MRC layers highly expressing MAdCAM-1 and TRANCE are observed at the outermost regions (arrows in *left* and *middle panels*). In the *right panels*, CD4$^+$CD3$^+$ mature T cells accumulate in the inner cortex (asterisks), while CD4$^+$CD3$^-$ cells are still present in the outer cortex (arrows). Note that MAdCAM-1 is still expressed by blood vessels even in peripheral LNs at this time. Bar, 200 μm.

began (Fig. 7*B*). The expression of MAdCAM-1 and TRANCE was markedly reduced in the developing paracortex and medulla, while the outermost part still retained high expression of the two molecules in conjunction with the colonization of CD4$^+$CD3$^-$ cells. These observations are consistent with the idea that, with the

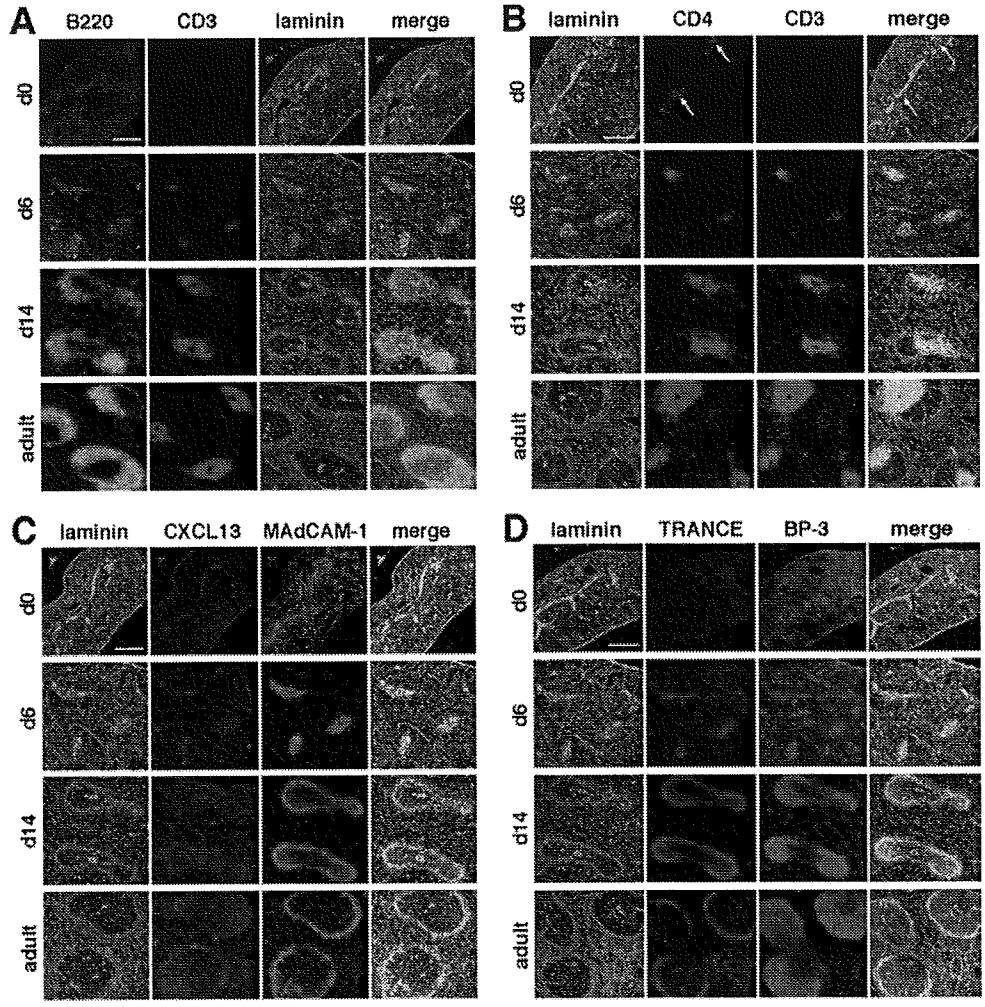

FIGURE 8. Development of the white pulp in spleen. Spleen sections from days 0, 6, and 14 and adult mice were stained for the indicated markers and examined by confocal microscopy. MRC layer/marginal sinus-lining structure expands and becomes prominent as lymphocytes are accumulated. In day 0 spleen, $CD4^+CD3^-$ LTi-like cells are concentrated at presumptive white pulp surrounding large blood vessels (arrows in *B*). Bars, 200 μm.

expansion of the organ, LTo stromal cells subsequently form a thin MRC layer in the tissue periphery.

An analogous process occurred in the area surrounding the central artery in the developing spleen, in which a stromal layer similar to LTo/MRCs expanded outward as lymphocytes accumulated in presumptive white pulp; eventually, this layer constituted the lining of the marginal sinus (Fig. 8). Interestingly, MAdCAM-1^+ mesenchymal cells showed relatively diffuse distribution in the day 0 spleen, but thereafter became concentrated around the artery at day 6 and then expanded to form the MRC layer. Accordingly, there is a dynamic redistribution of MRC lineage in the developing spleen.

Maintenance of MRC property requires LTβR signaling

To address the role of LTβR signaling in the maintenance of the MRC layer in mature SLOs, LTβR-Fc chimeric protein was injected into adult mice, and SLOs were examined after 2–4 wk of weekly administration of the chimeric proteins. No discernable alterations in the architecture of SLOs were observed in control experiments in which mice were injected with II-6 TCRVα-Fc chimeric protein (30) or PBS compared with untreated animals (Fig. 9 and data not shown). Consistent with previous reports, the structure of splenic white pulp (in particular, follicular assembly) was disorganized as a result of LTβR-Fc treatment (35, 36) (Fig. 9*A*). FDC networks also disappeared (data not shown). LTβR-Fc treatment abolished MAdCAM-1 expression and the typical boundary structure of the marginal sinus, which also caused the complete disappearance of the MRC layer highlighted by CXCL13, TRANCE, and BP-3 staining. Similar views were obtained in the spleen in *aly/aly* mice, which bear a point mutation in NIK (37) (Fig. 9*A*), and the observations are in good accordance with a previous report showing the absence of sinus-lining FRCs and MAdCAM-1 expression in the *aly/aly* spleen (38). These data indicate that the maintenance of the MRC layer in the spleen strongly depends on LTβR-NIK signaling.

Although LTβR-Fc treatment dramatically diminished the expression of CXCL13 and MAdCAM-1 in the MRC layer of the LNs, TRANCE expression was comparable to or slightly reduced compared with that in control LNs; furthermore, we found no remarkable alteration in the structure of the SCS (Fig. 9*B*). As FDC networks indicated by CR1 and FDC-M2, which are highly depending on LTβR signaling, disappeared (data not shown), circulating LTβR-Fc protein was suggested to reach a high enough level to block the pathway. This suggests that TRANCE expression in MRCs is independent of LTβR-signaling or another TRANCE-expressing cell types still exist in the case of LNs, although some MRC properties still depend on this pathway. It is also clear that the LTβR dependence in MRC layers differs among SLOs.

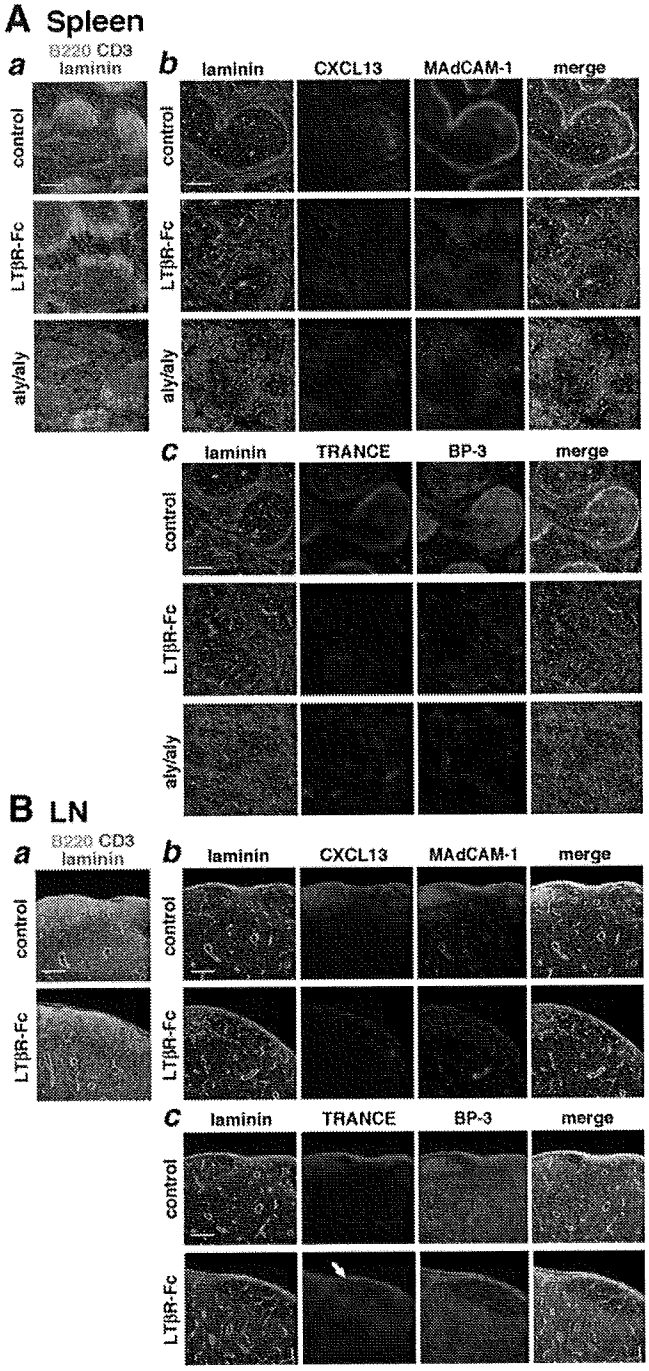

FIGURE 9. LTβR signaling is involved in the maintenance of MRC features. *A*, Inhibition of LTβR signaling or the absence of NIK activity abolishes MRC layer/marginal sinus-lining structure in the splenic white pulp. Spleens from control (Vα-Fc)-treated mice, LTβR-Fc-treated mice, or *aly/aly* mice were examined for the indicated markers. Representative images for the localization of T and B cells (*a*) and stromal structures (*b* and *c*) in each experiment are shown. MRC layers are absent in LTβR-Fc-treated or *aly/aly* mice spleen. Follicular structures are severely disorganized as well (*a*). *B*, Inhibition of LTβR signaling abolishes some markers but has little influence on TRANCE expression in LN MRCs. LN sections from control (Vα-Fc)- or LTβR-Fc-treated mice were examined for the indicated markers. Substantial expression of TRANCE is still retained in the MRC layer of LTβR-Fc-treated mice (arrow). Bars, 200 μm.

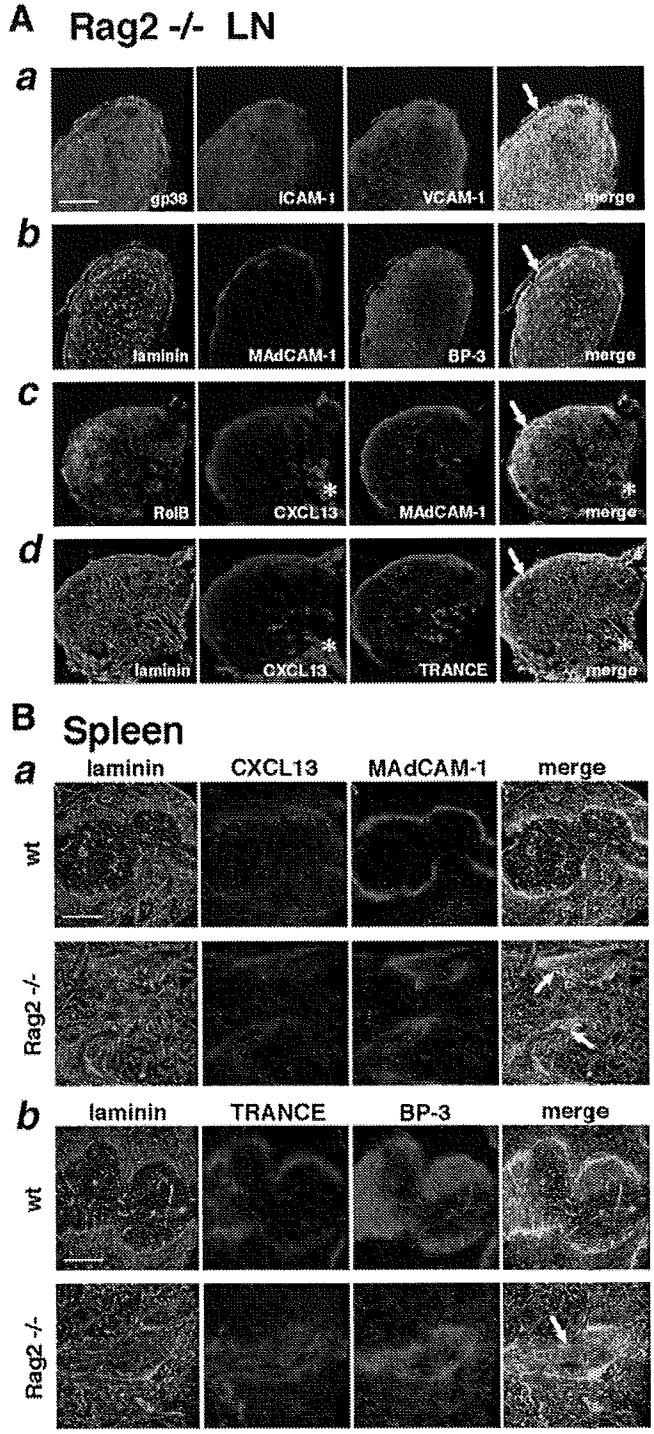

FIGURE 10. MRC layer is present in Rag2$^{-/-}$ mice SLOs. *A*, Stromal cells expressing MRC markers can be observed at the SCS lining in the rudimental LNs of Rag2$^{-/-}$ mice (arrows). Peripheral LNs from Rag2$^{-/-}$ mice were examined for the indicated markers. Adipose tissues attached to the LNs are nonspecifically stained by anti-CXCL13 Ab (asterisks). *B*, Stromal sacks that express MRC markers are observed at the rudimentary white pulp surrounding the central splenic artery in Rag2$^{-/-}$ mice (arrows). Spleens from wild-type (wt) and Rag2$^{-/-}$ mice were examined for the indicated markers. Bars, 200 μm.

Lymphocytes are dispensable for the formation of MRC layer

To address whether lymphocytes are required for the MRCs in adult SLOs, we next examined Rag2$^{-/-}$ mice. Rag2$^{-/-}$ mice have rudimentary LNs due to the lack of lymphocytes; nonetheless, we could clearly observe the MRC layer in the subcapsular region of each LN, in which weak but significant expression of CXCL13 was present (Fig. 10*A*). Thus, at least two compartments, i.e., the MRC layer and inner stroma, are unambiguously formed even in

the LNs from lymphocyte-deficient animals. Likewise, we observed reduced but significant expression of MRC markers at the sheath-like stromal structure surrounding the artery in the $Rag2^{-/-}$ mice spleen (Fig. 10*B*). These findings indicate that lymphocytes are not essential for the differentiation and maintenance of MRCs.

Discussion

In this study, the characterization of the lymphoid stromal cell line BLS12 prompted us to notice a unique lymphoid stromal population, MRC. MRC could be classified into a novel category of mesenchymal lineage common to adult SLOs, defined as the population of specialized reticular fibroblasts localized at a particular area of the tissues. These cells exhibit high expression of VCAM-1, ICAM-1, MAdCAM-1, CXCL13, TRANCE, BP-3, and gp38, as well as various reticular matrix components. Although FDCs show a similar marker set, they exhibit high expression of CR1 but low or no TRANCE, whereas MRCs express TRANCE but little or no CR1. Furthermore, FDCs do not generally produce typical reticular structure such as the one that surrounds the ECM fiber to form the conduit. Since the phenotypical characteristic of BLS12 shows good agreement with the criteria for MRC, we consider this cell line to be of MRC origin. However, there are some discrepancies between the nature of BLS12 and MRCs. For instance, BLS12 cells in culture constitutively display VCAM-1, ICAM-1, and MAdCAM-1, whereas in vivo the expression of these molecules is regulated by LTβR signaling. In addition, TRANCE protein is undetectable in BLS12, although TRANCE mRNA is readily detected. Immortalization and expansion in vitro presumably caused these alterations in BLS12.

Now that MRCs have been added to the list of stromal cells, every SLO turns out to be composed of at least three different types of mesenchymal stromal cells, i.e., FRCs in T zone, FDCs, and MRCs. Among these, the former two, FRCs expressing CCL19/CCL21 in the T zone and FDCs expressing CXCL13 in the follicular center, have been established as major anatomical backbones for the T and B compartments, respectively (7). It was recently demonstrated that these stromal networks support lymphocyte movement, acting as guidance footholds (39). Although the medulla of LNs and the marginal zone of the spleen are supported by types of FRC subsets distinct from those in the T zone (3, 14), these populations are not to be included in the common elements because they reside in varying anatomical compartments depending on SLO type. T zone FRCs and follicular FDCs are closely associated with the corresponding lymphocyte subsets. In addition, both of these types of stromal cells are induced in chronic inflammatory diseases, even in ectopic lymphoid tissues (30, 33, 40, 41). Therefore, we would suggest that the existence of mature lymphocytes induces the differentiation and maintenance of these stromal cells. In accordance with this, no obvious subcompartments supported by these stromal lineages are observed in $Rag2^{-/-}$ mice SLOs, whereas adoptive transfer of lymphocytes restores them (Ref. 1 and our unpublished observation). In contrast, MRCs are probably present in all SLOs, even in $Rag^{-/-}$ mice, but absent in ectopic lymphoid tissues, strongly supporting the notion that MRCs are a developmentally programmed element and tightly fixed to the organ, irrespective of the existence of mature lymphocytes. This notion is consistent with previous observations that organogenesis and even some tissue compartmentalization of SLOs, possibly concomitant with the separation of MRCs from other stromal cells, can occur in SCID mice (42–44).

The fact that MRCs display the set of molecular markers that is also expressed by LTo cells suggests the relevance of them. Indeed, we observed that LTo descendants in the outer margin of the LN anlagen seem to subsequently form the MRC layer. Likewise, periarteriolar LTo-like sheaths in the neonatal spleen gradually expand to form MRC rings, previously known as marginal sinus-lining cells. These observations prompt us to speculate that the organizer-like stromal cells are still present as MRCs in mature SLOs. MRC-like cells are also observed in the apical dome region of mucosal-associated lymphoid organs. These are likely the same cells reported previously as $TRANCE^{+}$ stromal cells in PPs, ILFs, and CPs (45). In general, CPs contain few lymphocytes but are colonized by LTi-like hematopoietic cells and the stromal cells exhibit characteristics similar to LTo/MRC (13, 46). It was recently suggested that ILFs are inducible structures derived from CP in response to the intestinal bacterial flora (13). Therefore, the maturation process of ILFs recapitulates the organogenesis of SLOs in the adult environment.

Based on the findings in this study and slightly modifying the models presented previously (10, 47), we propose following four sequential stages of SLO organogenesis from anatomical and stromal viewpoints (Fig. 11). In the earliest phase (stage I), a developmentally programmed "address code" determines the location of anlagen by attracting LTi cells or converting the adjacent mesenchyme to LTo congregates. Cross-talk between LTi and LTo cells facilitates the maturation of LTo stroma, which further drives a positive feedback loop. As anlagen grow (stage II), the stromal network differentiates into outer (genuine LTo layer?) and inner (presumptive lymphocyte compartment) parts (primary differentiation and compartmentalization of stromal cells). Hashi et al. (43) demonstrated the compartmentalization of the PP anlagen before lymphocyte entry and several other reports also have presented clear pictures showing uneven distributions of LTo and LTi cells within the SLO anlagen (22, 34). After birth (stage III), the influx of lymphocytes begins and the inner part of anlagen is further divided into lymphocyte subcompartments with corresponding adult stromal subsets (secondary differentiation and compartmentalization of stromal cells); meanwhile, the outermost part expands to form the MRC layer. Tissue architecture (stage IV) is maturated in the adult SLO. Continuous LTβR signaling is required for maintenance of the properties of MRCs; however, the dependence on this pathway varies depending on the individual SLO. The administration of LTβR-Fc completely disrupts the marginal sinus structure, with loss of the MRC layer in the splenic white pulp, although this treatment does not lead to the immediate disappearance of the white pulp structure. Likewise, LTβR-Fc partially diminishes markers in LN MRCs, but has little effect on TRANCE expression or overall tissue geometry, suggesting that MRCs are dispensable for the accumulation and compartmentalization of lymphocytes, at least once the construction of SLO architecture has been accomplished.

Although the functional significance of MRCs in adult SLOs remains largely unknown, we consider it important to note that all MRC layers in various SLOs are faced toward the major route of antigenic entry (Fig. 11). DCs capturing Ags in peripheral tissues migrate to the draining LNs via afferent lymph. They first reach the SCS, from which they pass across the MRC layer to enter the paracortex (48). Low-molecular weight soluble Ags can pass the SCS lining, penetrating into the conduit network in the T zone, where they can be picked up by resident DCs (5, 6). Analogously, MRC networks in the subepithelial dome of mucosal SLOs harbor unique DC subsets by which Ags are transported from the FAE to the follicular region (49, 50). In the spleen, blood-borne Ags and immune cells must pass through the marginal stromal layer to enter the inner lymphoid compartment of the white pulp (14). Accordingly, the MRC layer possibly regulates these Ag-transporting pathways. Of note along these lines, follicular B cells in the LN

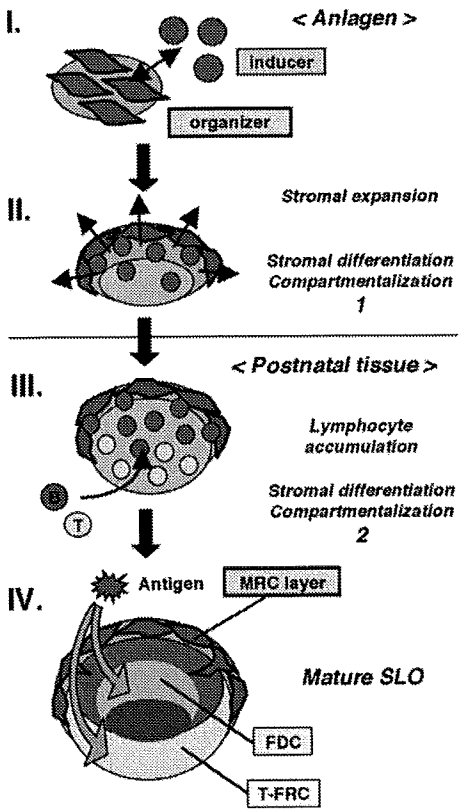

FIGURE 11. A common model for SLO oraganogenesis that progresses through four sequential stages. Stage I: In the earliest step, intimate interaction between organizer mesenchyme and inducer cells forms the SLO anlagen, under the control of an address code specific in embryonic environment. Stage II: As the anlage grows, the stromal compartment is gradually segregated into outer and inner parts, i.e., the presumptive MRC layer and lymphocyte compartments, respectively (primary differentiation and compartmentalization of stromal cells). Stromal cells in the outer part show the organizer phenotype more remarkably. Stage III: After birth, lymphocytes are accumulated in the inner area, in which they are further separated into outer (B cells) and inner (T cells) areas with the differentiation of corresponding stromal lineages (secondary differentiation and compartmentalization of stromal cells); meanwhile, the outermost stromal population proceeds to expand and eventually forms the MRC layer. B cells in the outer cortex are further assembled to form follicles. Stage IV: Mature architecture of adult SLO. In response to antigenic stimuli, a germinal center is occasionally developed in the follicle, with the asymmetry of dark and light zones. Note that common stromal elements in mature SLOs are MRCs, FDCs, and T zone FRCs. Regular tissue architecture is arranged along with a polarity axis directed toward the major route of Ag entry.

directly capture lymph-borne Ags, either in a soluble form penetrated from the SCS or in a particulate form from SCS-resident cells (51–54). As the network of MRCs covers the outer part of the follicle, MRCs are likely to be involved in the Ag transport along this route. It is also likely that the MRC network is the foothold for the migration of B cells in the outer follicle. Intravital two-photon microscopy has shown that B cells in this region are highly motile (52, 53). Lo et al. (55) have demonstrated that lymphocyte entry into the splenic white pulp across the marginal sinus is integrin and Gαi dependent. High expression of adhesion molecules in MRCs suggests that their network represents a potential foothold not only for B cells but also for macrophages and DCs. In fact, BLS12 cells display various adhesion molecules and constitutively produce CXCL12; they express CXCL13 in response to LTβR signaling. BLS12 also supports the migration of primary B cells in vitro, which partially depends on Gαi-mediated signaling and integrins. However, recent studies have shown that integrins are not the major adhesion machinery, at least for the interstitial migration of T cells and DCs within the LN (56, 57). Careful examination of the integrin requirement for the migration of B cells in this area will be required in future studies.

In summary, the MRC layer is a common landmark of mature SLOs; these stromal cells are presumably the adult counterpart of LTo. The organogenesis of SLOs proceeds like a layer-forming reaction. Supposing the LTo/MRC layer as the organizing front of developing SLOs, this is quite reasonable, because the anatomical arrangement of SLOs must necessarily be optimized for capturing and detecting external Ags most efficiently. Since there are multiple mesenchymal lineages, each with distinct functions, tightly integrated into tissue microanatomy, tracing stromal components during the organogenesis and remodeling of SLOs is a suitable system for studying the specialization and diversification of mesenchymal cells via close interaction with lymphoid or myeloid cells. BLS12 cells will be a unique and highly valuable tool for exploring the cytological and biochemical nature of lymphoid stromal cells.

Acknowledgments

We thank W. C. Greene for NIK cDNA, A. G. Farr for anti-gp38 Ab, M. D. Cooper for anti-BP-3 Ab, M. H. Kosco-Vilbois for anti-FDC-M2 Ab, and T. Gonda-Ohfiji, K. Araki, and T. Hayashi for technical assistance.

Disclosures

The authors have no financial conflict of interest.

References

1. Fu, Y. X., and D. D. Chaplin. 1999. Development and maturation of secondary lymphoid tissues. *Annu. Rev. Immunol.* 17: 399–433.
2. Gretz, J. E., A. O. Anderson, and S. Shaw. 1997. Cords, channels, corridors, and conduits: critical architectural elements facilitating cell interactions in the lymph node cortex. *Immunol. Rev.* 156: 11–24.
3. Katakai, T., T. Hara, J. H. Lee, H. Gonda, M. Sugai, and A. Shimizu. 2004. A novel reticular stromal structure in lymph node cortex: an immuno-platform for interactions among dendritic cells, T cells, and B cells. *Int. Immunol.* 16: 1133–1142.
4. Katakai, T., T. Hara, M. Sugai, H. Gonda, and A. Shimizu. 2004. Lymph node fibroblastic reticular cells construct the stromal reticulum via contact with lymphocytes. *J. Exp. Med.* 200: 783–795.
5. Gretz, J. E., C. C. Norbury, A. O. Anderson, A. E. Proudfoot, and S. Shaw. 2000. Lymph-borne chemokines and other low molecular weight molecules reach high endothelial venules via specialized conduits while a functional barrier limits access to the lymphocyte microenvironments in lymph node cortex. *J. Exp. Med.* 192: 1425–1440.
6. Sixt, M., N. Kanazawa, M. Selg, T. Samson, G. Roos, D. P. Reinhardt, R. Pabst, M. B. Lutz, and L. Sorokin. 2005. The conduit system transports soluble antigens from the afferent lymph to resident dendritic cells in the T cell area of the lymph node. *Immunity* 22: 19–29.
7. Cyster, J. G. 1999. Chemokines and cell migration in secondary lymphoid organs. *Science* 286: 2098–2102.
8. Cyster, J. G., K. M. Ansel, K. Reif, E. H. Ekland, P. L. Hyman, H. L. Tang, S. A. Luther, and V. N. Ngo. 2000. Follicular stromal cells and lymphocyte homing to follicles. *Immunol. Rev.* 176: 181–193.
9. Luther, S. A., H. L. Tang, P. L. Hyman, A. G. Farr, and J. G. Cyster. 2000. Coexpression of the chemokines ELC and SLC by T zone stromal cells and deletion of the ELC gene in the *plt/plt* mouse. *Proc. Natl. Acad. Sci. USA* 97: 12694–12699.
10. Nishikawa, S., K. Honda, P. Vieira, and H. Yoshida. 2003. Organogenesis of peripheral lymphoid organs. *Immunol. Rev.* 195: 72–80.
11. Mebius, R. E. 2003. Organogenesis of lymphoid tissues. *Nat. Rev. Immunol.* 3: 292–303.
12. Kiyono, H., and S. Fukuyama. 2004. NALT- versus Peyer's-patch-mediated mucosal immunity. *Nat. Rev. Immunol.* 4: 699–710.
13. Eberl, G. 2005. Inducible lymphoid tissues in the adult gut: recapitulation of a fetal developmental pathway? *Nat. Rev. Immunol.* 5: 413–420.
14. Mebius, R. E., and G. Kraal. 2005. Structure and function of the spleen. *Nat. Rev. Immunol.* 5: 606–616.
15. Mebius, R. E., P. Rennert, and I. L. Weissman. 1997. Developing lymph nodes collect $CD4^+CD3^-$ $LT\beta^+$ cells that can differentiate to APC, NK cells, and follicular cells but not T or B cells. *Immunity* 7: 493–504.
16. Yoshida, H., K. Honda, R. Shinkura, S. Adachi, S. Nishikawa, K. Maki, K. Ikuta, and S. I. Nishikawa. 1999. IL-7 receptor α^+ $CD3^-$ cells in the embryonic intestine induces the organizing center of Peyer's patches. *Int. Immunol.* 11: 643–655.

17. Honda, K., H. Nakano, H. Yoshida, S. Nishikawa, P. Rennert, K. Ikuta, M. Tamechika, K. Yamaguchi, T. Fukumoto, T. Chiba, and S. I. Nishikawa. 2001. Molecular basis for hematopoietic/mesenchymal interaction during initiation of Peyer's patch organogenesis. *J. Exp. Med.* 193: 621–630.
18. Finke, D., H. Acha-Orbea, A. Mattis, M. Lipp, and J. Kraehenbuhl. 2002. $CD4^+CD3^-$ cells induce Peyer's patch development: role of $\alpha_4\beta_1$ integrin activation by CXCR5. *Immunity* 17: 363–373.
19. Weih, F., and J. Caamano. 2003. Regulation of secondary lymphoid organ development by the nuclear factor-κB signal transduction pathway. *Immunol. Rev.* 195: 91–105.
20. Yokota, Y., A. Mansouri, S. Mori, S. Sugawara, S. Adachi, S. Nishikawa, and P. Gruss. 1999. Development of peripheral lymphoid organs and natural killer cells depends on the helix-loop-helix inhibitor Id2. *Nature* 397: 702–706.
21. Sun, Z., D. Unutmaz, Y. R. Zou, M. J. Sunshine, A. Pierani, S. Brenner-Morton, R. E. Mebius, and D. R. Littman. 2000. Requirement for RORγ in thymocyte survival and lymphoid organ development. *Science* 288: 2369–2373.
22. Eberl, G., S. Marmon, M. J. Sunshine, P. D. Rennert, Y. Choi, and D. R. Littman. 2004. An essential function for the nuclear receptor RORγt in the generation of fetal lymphoid tissue inducer cells. *Nat. Immunol.* 5: 64–73.
23. Kim, D., R. E. Mebius, J. D. MacMicking, S. Jung, T. Cupedo, Y. Castellanos, J. Rho, B. R. Wong, R. Josien, N. Kim, et al. 2000. Regulation of peripheral lymph node genesis by the tumor necrosis factor family member TRANCE. *J. Exp. Med.* 192: 1467–1478.
24. Kong, Y. Y., H. Yoshida, I. Sarosi, H. L. Tan, E. Timms, C. Capparelli, S. Morony, A. J. Oliveira-dos-Santos, G. Van, A. Itie, et al. 1999. OPGL is a key regulator of osteoclastogenesis, lymphocyte development and lymph-node organogenesis. *Nature* 397: 315–323.
25. Dougall, W. C., M. Glaccum, K. Charrier, K. Rohrbach, K. Brasel, T. De Smedt, E. Daro, J. Smith, M. E. Tometsko, C. R. Maliszewski, et al. 1999. RANK is essential for osteoclast and lymph node development. *Genes Dev.* 13: 2412–2424.
26. Yoshida, H., A. Naito, J. Inoue, M. Satoh, S. M. Santee-Cooper, C. F. Ware, A. Togawa, S. Nishikawa, and S. Nishikawa. 2002. Different cytokines induce surface lymphotoxin-$\alpha\beta$ on IL-7 receptor-α cells that differentially engender lymph nodes and Peyer's patches. *Immunity* 17: 823–833.
27. Farr, A. G., M. L. Berry, A. Kim, A. J. Nelson, M. P. Welch, and A. Aruffo. 1992. Characterization and cloning of a novel glycoprotein expressed by stromal cells in T-dependent areas of peripheral lymphoid tissues. *J. Exp. Med.* 176: 1477–1482.
28. Berney, C., S. Herren, C. A. Power, S. Gordon, L. Martinez-Pomares, and M. H. Kosco-Vilbois. 1999. A member of the dendritic cell family that enters B cell follicles and stimulates primary antibody responses identified by a mannose receptor fusion protein. *J. Exp. Med.* 190: 851–860.
29. McNagny, K. M., R. P. Bucy, and M. D. Cooper. 1991. Reticular cells in peripheral lymphoid tissues express the phosphatidylinositol-linked BP-3 antigen. *Eur. J. Immunol.* 21: 509–515.
30. Katakai, T., T. Nomura, H. Gonda, M. Sugai, Y. Agata, A. Nishio, T. Masuda, S. Sakaguchi, and A. Shimizu. 2006. Spontaneous large-scale lymphoid neogenesis and balanced autoimmunity versus tolerance in the stomach of H^+/K^+-ATPase-reactive TCR transgenic mouse. *J. Immunol.* 177: 7858–7867.
31. Katagiri, K., A. Maeda, M. Shimonaka, and T. Kinashi. 2003. RAPL, a Rap1-binding molecule that mediates Rap1-induced adhesion through spatial regulator of LFA-1. *Nat. Immunol.* 4: 741–748.
32. Sukumar, S., A. K. Szakal, and J. G. Tew. 2006. Isolation of functionally active murine follicular dendritic cells. *J. Immunol. Methods* 313: 81–95.
33. Katakai, T., T. Hara, M. Sugai, H. Gonda, and A. Shimizu. 2003. Th1-biased tertiary lymphoid tissue supported by CXC chemokine ligand 13-producing stromal network in chronic lesions of autoimmune gastritis. *J. Immunol.* 171: 4359–4368.
34. Cupedo, T., M. F. Vondenhoff, E. J. Heeregrave, A. E. De Weerd, W. Jansen, D. G. Jackson, G. Kraal, and R. E. Mebius. 2004. Presumptive lymph node organizers are differentially represented in developing mesenteric and peripheral nodes. *J. Immunol.* 173: 2968–2975.
35. Rennert, P. D., J. L. Browning, R. Mebius, F. Mackay, and P. S. Hochman. 1996. Surface lymphotoxin α/β complex is required for the development of peripheral lymphoid organs. *J. Exp. Med.* 184: 1999–2006.
36. Rennert, P. D., D. James, F. Mackay, J. L. Browning, and P. S. Hochman. 1998. Lymph node genesis is induced by signaling through the lymphotoxin β receptor. *Immunity* 9: 71–79.
37. Shinkura, R., K. Kitada, F. Matsuda, K. Tashiro, K. Ikuta, M. Suzuki, K. Kogishi, T. Serikawa, and T. Honjo. 1999. Alymphoplasia is caused by a point mutation in the mouse gene encoding NF-κB-inducing kinase. *Nat. Genet.* 22: 74–77.
38. Koike, R., T. Nishimura, R. Yasumizu, H. Tanaka, Y. Hataba, T. Watanabe, S. Miyawaki, and M. Miyasaka. 1996. The splenic marginal zone is absent in alymphoplastic *aly* mutant mice. *Eur. J. Immunol.* 26: 669–675.
39. Bajénoff, M., J. G. Egen, L. Y. Koo, J. P. Laugier, F. Brau, N. Glaichenhaus, and R. N. Germain. 2006. Stromal cell networks regulate lymphocyte entry, migration, and territoriality in lymph nodes. *Immunity* 25: 989–1001.
40. Luther, S. A., T. Lopez, W. Bai, D. Hanahan, and J. G. Cyster. 2000. BLC expression in pancreatic islets cause B cell recruitment and lymphotoxin-dependent lymphoid neogenesis. *Immunity* 12: 471–481.
41. Aloisi, F., and R. Pujol-Borrell. 2006. Lymphoid neogenesis in chronic inflammatory diseases. *Nat. Rev. Immunol.* 6: 205–217.
42. Gonzalez, M., F. Mackay, J. L. Browning, M. H. Kosco-Vilbois, and R. J. Noelle. 1998. The sequential role of lymphotoxin and B cells in the development of splenic follicles. *J. Exp. Med.* 187: 997–1007.
43. Hashi, H., H. Yoshida, K. Honda, S. Fraser, H. Kubo, M. Awane, A. Takabayashi, H. Nakano, Y. Yamaoka, and S. Nishikawa. 2001. Compartmentalization of Peyer's patch anlagen before lymphocyte entry. *J. Immunol.* 166: 3702–3709.
44. Cupedo, T., F. E. Lund, V. N. Ngo, T. D. Randall, W. Jansen, M. J. Greuter, R. de Waal-Malefyt, G. Kraal, J. G. Cyster, and R. E. Mebius. 2004. Initiation of cellular organization in lymph nodes is regulated by non-B cell-derived signals and is not dependent on CXC chemokine ligand 13. *J. Immunol.* 173: 4889–4896.
45. Taylor, R. T., S. R. Patel, E. Lin, B. R. Butler, J. G. Lake, R. D. Newberry, and I. R. Williams. 2007. Lymphotoxin-independent expression of TNF-related activation-induced cytokine by stromal cells in cryptopatches, isolated lymphoid follicles, and Peyer's patches. *J. Immunol.* 178: 5659–5667.
46. Kanamori, Y., K. Ishimaru, M. Nanno, K. Maki, K. Ikuta, H. Nariuchi, and H. Ishikawa. 1996. Identification of novel lymphoid tissues in murine intestinal mucosa where clusters of $c\text{-}kit^+IL\text{-}7R^+Thy1^+$ lympho-hemopoietic progenitors develop. *J. Exp. Med.* 184: 1449–1459.
47. Cupedo, T., and R. E. Mebius. 2005. Cellular interactions in lymph node development. *J. Immunol.* 174: 21–25.
48. Itano, A. A., and M.K. Jenkins. 2003. Antigen presentation to naive CD4 T cells in the lymph node. *Nat. Immunol.* 4: 733–739.
49. Iwasaki, A., and B. L. Kelsall. 2000. Localization of distinct Peyer's patch dendritic cell subsets and their recruitment by chemokines macrophage inflammatory protein (MIP)-3α, MIP-3β, and secondary lymphoid organ chemokine. *J. Exp. Med.* 191: 1381–1394.
50. Mowat, A. M. 2003. Anatomical basis of tolerance and immunity to intestinal antigens. *Nat. Rev. Immunol.* 3: 331–341.
51. Pape, K. A., D. M. Catron, A. A. Itano, and M. K. Jenkins. 2007. The humoral immune response is initiated in lymph nodes by B cells that acquire soluble antigen directly in the follicles. *Immunity* 26: 491–502.
52. Carrasco, Y. R., and F. D. Batista. 2007. B cells acquire particulate antigen in a macrophage-rich area at the boundary between the follicle and the subcapsular sinus of the lymph node. *Immunity* 27: 160–171.
53. Phan, T. G., I. Grigorova, T. Okada, and J. G. Cyster. 2007. Subcapsular encounter and complement-dependent transport of immune complexes by lymph node B cells. *Nat. Immunol.* 8: 992–1000.
54. Junt, T., E. A. Moseman, M. Iannacone, S. Massberg, P. A. Lang, M. Boes, K. Fink, S. E. Henrickson, D. M. Shayakhmetov, N. C. Di Paolo, et al. 2007. Subcapsular sinus macrophages in lymph nodes clear lymph-borne viruses and present them to antiviral B cells. *Nature* 450: 110–114.
55. Lo, C. G., T. T. Lu, and J. G. Cyster. 2003. Integrin-dependence of lymphocyte entry into the splenic white pulp. *J. Exp. Med.* 197: 356–361.
56. Woolf, E., I. Grigorova, A. Sagiv, V. Grabovsky, S. W. Feigelson, Z. Shulman, T. Hartmann, M. Sixt, J. G. Cyster, and R. Alon. 2007. Lymph node chemokines promote sustained T lymphocyte motility without triggering stable integrin adhesiveness in the absence of shear forces. *Nat. Immunol.* 8: 1076–1085.
57. Lämmermann, T., B. L. Bader, S. J. Monkley, T. Worbs, R. Wedlich-Söldner, K. Hirsch, M. Keller, R. Förster, D. R. Critchley, R. Fässler, and M. Sixt. 2008. Rapid leukocyte migration by integrin-independent flowing and squeezing. *Nature* 453: 51–55.